MATERIALS SCIENCE AND ENGINEERING

Director's R&D Fund

Creating Oxygen-Rich Nanoclusters for High-Temperature Strengthening of Structural Alloys

D. T. Hoelzer,[1] P. J. Maziasz,[1] S. S. Babu,[1] M. K. Miller,[1] C-L. Fu,[1] E. A. Kenik,[1]
I. G. Wright,[1] E. D. Specht,[1] and J. L. Robertson[2]
[1]*Metals and Ceramics Division*
[2]*Condensed Matter Sciences Division*

The goal of this project was to develop the understanding of a new phenomenon involving the formation of a high-number density of uniformly dispersed nanoscale oxygen-rich clusters in an iron-based alloy. The technological impact of forming the nanoscale oxygen-rich clusters is that the high-temperature strength and creep resistance of the iron alloy is significantly enhanced. The scientific impact challenges our current understanding of the stability of oxide phases in metallic systems. An experimental and theory/modeling effort was developed to investigate the evolution from the meso-scale oxide structure to the nanoscale clusters and to expand the current scientific knowledge of non-equilibrium thermodynamics, phase formation and stability, and nanoscale strengthening mechanisms at high temperatures. This understanding may also lead to new alloy design and alternative processing methods to produce a range of advanced structural alloys with superior high-temperature performance.

Introduction

New structural materials possessing significantly improved high-temperature, high-strength properties are required to meet future goals for higher thermal efficiencies in energy generation systems. One approach for achieving these requirements is to disperse oxide particles in the alloy matrix, which improves the high-temperature creep resistance by acting as hard obstacles that hinder the motion of dislocations and grain boundaries. Historically, the mechanical alloying (MA) approach has been used to disperse oxide particles in the matrix of many technologically important alloy systems, such as aluminum, iron, and nickel, to increase the high-temperature mechanical strength properties. These advanced materials are usually referred to as oxide dispersion strengthened (ODS) alloys.

Mechanical alloying has been used for more than 30 years to make commercial ODS alloys and for basic research studies.[1] This process involves ball milling metallic or pre-alloyed powders with the dispersoid powder, such as Y_2O_3, and then consolidating the powders into a bulk shape. In the past, the general understanding of MA is that it essentially "mixes" the alloy and dispersoid powders by mechanical means. Very few studies focused on the structural and chemical evolution of the dispersoid during ball milling. However, in the late 1990s, a new phenomenon involving a high-number density of nanosize clusters containing Y, Ti, and O atoms was discovered in a mechanically alloyed (MA) Fe-12Cr-3W-0.4Ti-0.25Y_2O_3 (wt %) iron alloy, referred to as 12YWT, that showed a remarkable improvement in high-temperature, high-strength properties.[2] This discovery has stimulated the importance of understanding the structural and chemical evolution of the initial oxide dispersoid to nanoclusters.

We believe that a study must comprise both experiment and theory to develop the understanding of nanosize clusters formation. Our primary focus was to investigate the structure and stability of the nanoclusters at high temperatures and to develop the understanding of how the stable yttria-oxide evolves into new nanoclusters in a model iron alloy during mechanical alloying (MA). This research project expanded the current scientific knowledge of non-equilibrium thermodynamics, phase formation and stability, and nanoscale strengthening mechanisms at high temperatures. We also foresee developing the knowledge for improving the MA processing method and for developing non-MA processing methods for achieving high-number densities of uniformly dispersed nanoclusters.

Technical Approach

Stability and Structure of Nanoclusters

Determining the salient properties of the nanoclusters was paramount to understanding the mechanisms for their formation. The approach was to investigate the nanoclusters, initially discovered in the 12YWT alloy, using advanced analytical techniques to obtain information regarding their unique structure, such as the crystal

structure, composition, and interfacial structure. These studies mainly included the atom probe tomography (APT) and advanced electron microscopy techniques but also included several attempts using different X-ray scattering techniques. The initial discovery of the nanoclusters was made on the as-processed 12YWT alloy, which was reportedly exposed to processing temperatures up to 1150ºC. This result suggested that the nanoclusters were stable at high temperature. In order to more clearly define the high-temperature stability of the nanoclusters, heat treatments were conducted on the 12YWT at temperatures as high as 1300ºC, which is higher than 85% of the melting point of this alloy.

Formation of Nanoclusters

Our experimental approach to forming nanoclusters in an iron-based alloy was largely based on information available regarding the composition and processing history that went into developing the 12YWT ferritic alloy. This information included the composition, ball milling conditions, and consolidation temperature, which was stated to be 1150ºC. High-quality, gas-atomized pre-alloyed Fe-14%Cr (wt %) powders containing systematic additions of 3%W, 0.4%Ti, and 3%W+0.4%Ti were procured for ball milling and powder consolidation studies. Four different alloy compositions were ball milled with the same concentration of Y_2O_3 used in 12YWT, which was 0.25%Y_2O_3. A fundamental study was first conducted on the ball milled powders using X-ray diffraction (XRD) and transmission electron microscopy (TEM) to study the effects of ball milling parameters and alloy composition on the structural evolution of Y_2O_3. The ball milled powders were then consolidated by hot extrusion at two temperatures; the first extrusion was conducted close to the reported consolidation temperature of the 12YWT alloy (1175ºC), and the second extrusion was conducted at a considerably lower temperature of 850ºC. Issues that were being explored centered mainly of the long-range diffusion of Y, Ti, and O in the iron matrix.

Theoretical Study

First-principles local-density-functional (LDF) theory was used to develop an understanding of conditions that favored nanocluster formation by focusing on the relationship among energetics, electronic structure, and bonding geometry of oxygen. Data collected from the APT studies provided significant information concerning the possible role of oxygen supersaturation as a mechanism for nanocluster formation. The goal of the theory was to answer why the unique combination of Y, Ti, and O is required for cluster formation. The theory examined the conditions under which the oxygen atoms are soluble in the Fe matrix in the presence of dissolved Ti and/or Y atoms without forming many stable oxide compounds. The model was successfully developed to also include the additional role of vacancies on the solubility of O in Fe.

Results and Accomplishments

Stability and Structure of Nanoclusters

Improving the maximum separation envelope (MSE) code was an important development in this project for analyzing the APT data on the nanoclusters.[3] This code is used for determining the atoms associated with a precipitate based on the principle that solute atoms in a precipitate are closer together than those in solid solution in the surrounding matrix because of differences in chemical bond strength. This permitted a more precise analysis of their size, number density, and composition. The composition of nanoclusters was consistently found to have a stoichiometric ratio of Ti and Y to O atoms close to 1:1 and to contain ~10–15 at % Fe atoms. However, the Ti, Y, and O atoms are not uniformly distributed in the nanoclusters.The radial concentration profile from the center of mass of the nanoclusters showed that their core is populated with Ti and O atoms, while the interface is enriched with Y atoms. This analysis also showed a diffuse interface, which could account for the apparent stability of the nanoclusters. Advanced electron microscopy techniques confirmed that the nanoclusters do not possess a unique crystal structure but that the atoms associated with them are clustered on the bcc lattice sites in the Fe matrix. However, the composition analysis of the matrix revealed an unusually high oxygen concentration that was more than 200 times the equilibrium solubility limit in bcc Fe at 800ºC.[4] These results led to questions about the structure and formation of nanoclusters that were addressed by theory and modeling.

Experiments consisting of creep testing for long times with an applied stress at temperatures up to 850ºC and for short-time exposures at temperatures up to 1300ºC revealed a remarkable degree of stability for the nanoclusters. In one significant creep test, the sample of 12YWT failed after ~14,500 h (~1.6 year) at 800°C and applied load of 138 MPa. This level of performance is several orders of magnitude better than that of any previously developed MA ODS Fe-Cr alloy. Surprisingly, as shown in Fig. 1, the APT analysis revealed essentially no change in the size, number density, and composition of the nanoclusters compared to the as-processed sample. Even exposures of 12YWT to extremely high temperatures of 1300ºC, which is ~86% of the melting point for this alloy, for up to 10 h did not significantly change the composition or size of the nanoclusters and only slightly changed their number density. Figure 2 shows a compilation of the data obtained for all of the nanoclusters analyzed in 12YWT after exposure to high-temperature environments.

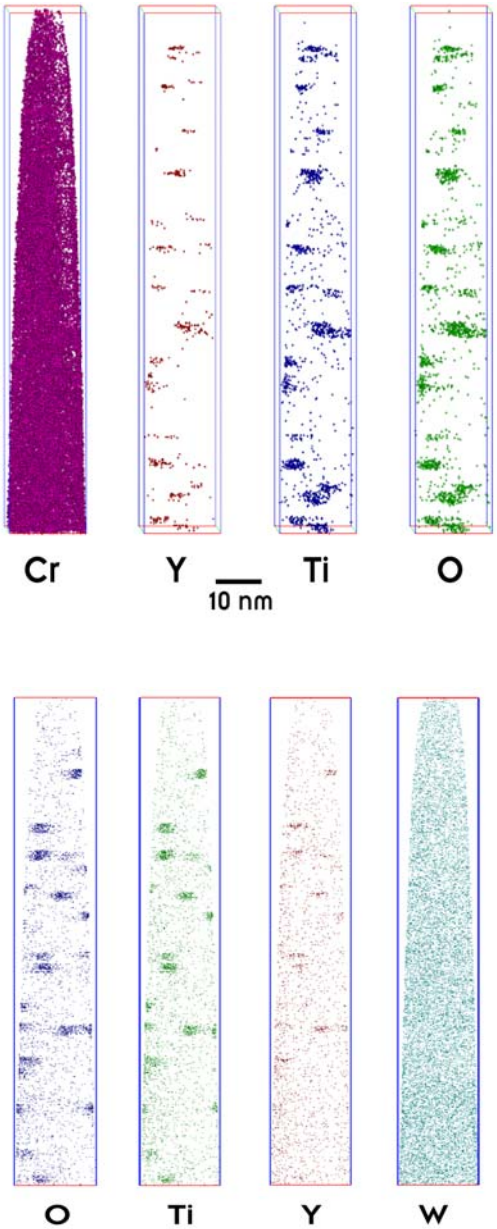

Figure 1. Three-dimensional atom probe tomography images of nanoclusters in 12YWT in (a) as-processed conditions and (b) after annealing at 1300ºC for 1hour.

Results obtained in this study regarding the structure and stability of nanoclusters challenge our understanding of some key areas in materials science. The most significant contribution to the materials science community is the result showing the amazing stability of the nanoclusters at extremely high temperatures of 1300ºC for up to 10 h. The results suggest that the nanoclusters are a metastable phase occupying the bcc lattice sites in the Fe matrix with a size range of less than ~4-nm diameter. According to thermodynamic laws, these characteristics

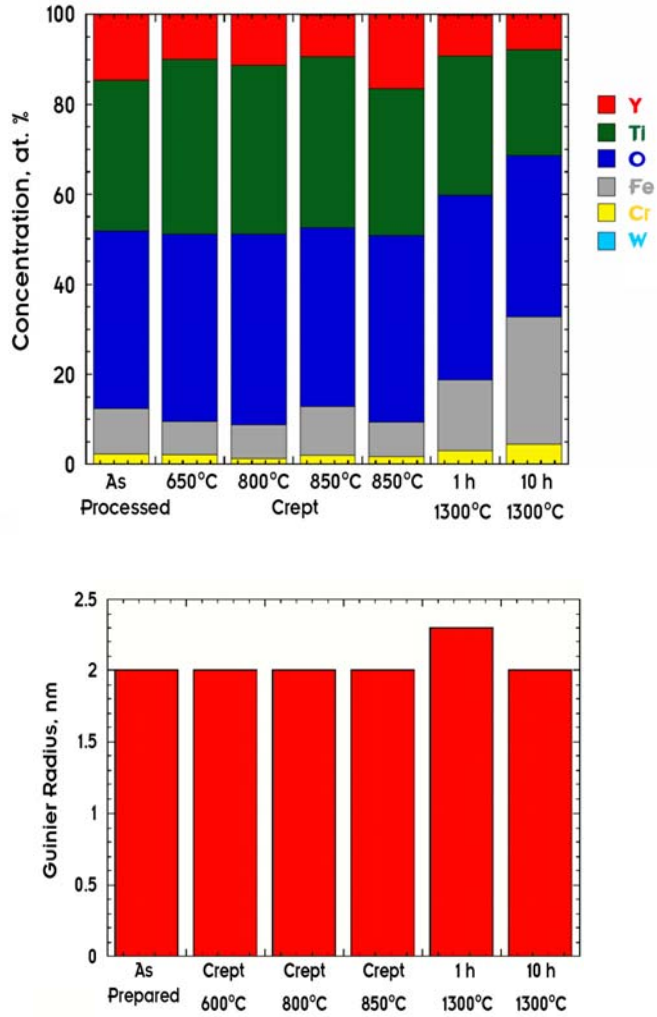

Figure 2. Atom probe tomography data showing essentially no changes in the (a) composition and (b) size of the nanoclusters in 12YWT upon exposure in long-time creep tests up to 850ºC and short-time high-temperature exposure at 1300ºC.

should result in rapid coarsening of size and in the transformation to an oxide compound at these high temperatures. Thus, this study has revealed a new concept of stable nanoclusters as a method for high-temperature strengthening of advanced structural materials.

Formation of Nanoclusters

Our fundamental study on ball milled powders of the model alloys demonstrated that the Y_2O_3 particles are reduced from an initial size of 17–31 nm to below ~2 nm and are forced into a nonequilibrium suspension in the bcc Fe matrix. The lower size limit was defined by the spatial resolution of the electron microscopy techniques that were employed. The composition of the powders had a minor effect on differences in the magnitude of internal lattice strain and final nanosize crystallite induced by ball milling, and had no significant effect on the evolution of the Y_2O_3 particles during ball milling.

A significant breakthrough was achieved in the investigation of consolidated powders. Our experimental results showed that the formation of nanosize particles occurs at low consolidation temperatures rather than at high temperatures. We first attempted to reproduce the extrusion conditions used for making the MA 12YWT alloy. However, extruding the four model alloys at 1175ºC resulted in the formation of a low number density of coarse oxide particles. The presence of Ti in two of the model alloys resulted in the formation of ternary Ti-, Y-, and O-based oxide particles that were slightly smaller in size and higher in number density compared to those in the two model alloys that did not contain Ti. These results indicated that the diffusion of Y and Ti atoms was too extensive at 1150ºC and higher, which favors large particles and a low nucleation rate. An extrusion temperature of 850ºC was then chosen based on the criteria of lowering the diffusion of Y and Ti atoms in the Fe matrix. This approach was successful in forming nanosize particles in the iron alloy containing both W (tungsten) and Ti, which is referred to as 14YWT. Figure 3 shows composition maps of the distribution of Fe (Fig. 3a) and Ti (Fig. 3b) atoms obtained by energy-filtered transmission electron microscopy (EFTEM). The darkly imaging particles in the Fe map are depleted in Fe and are enriched in Ti, which are brightly imaging particles in the Ti map. The formation of the particles was both inter- and transgranular with sizes as small as the detection limit of ~2 nm. The APT has revealed that the particles are enriched in Y, Ti, and O atoms similar to the nanoclusters discovered in the 12YWT alloy. Contrary to what was previously known about the processing conditions for the 12YWT, the results of this study establish low-temperature consolidation temperatures that minimize diffusion of critical elements such as Ti and Y as being significant for forming nanoclusters in iron-based alloys.

Theoretical Study

A theoretical model of the mechanism for forming Ti-Y-O-Fe-enriched nanoclusters in iron was developed in this study. The model is consistent with experimental results and describes the balance between the increase in strain energy and the gain in electronic bonding energy with Y, Ti, and O atoms in the bcc-Fe lattice. Critical factors for nucleating the nanoclusters have been identified from the model. It is believed that validation of the factors in a carefully designed experiment can form the basis of a patent for developing nanoclusters in iron-based as well as other technically important alloy systems.

Summary and Conclusions

In summary, we determined that a very high number density of "nanoclusters" that formed in the mechanically

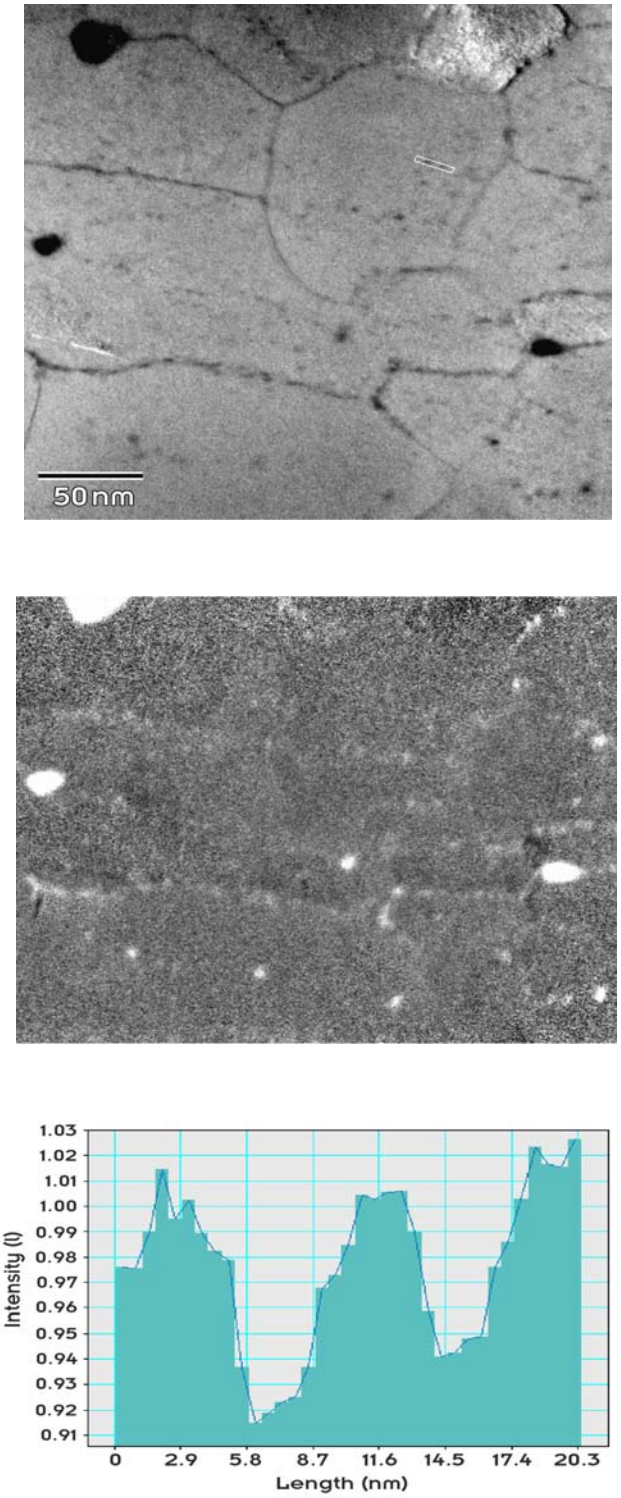

Figure 3. Energy filtered TEM images showing nanoclusters in the 14YWT alloy that was extruded at 850ºC. The nanoclusters are dark in the Fe jump ratio map (a) and bright in the Ti jump ratio map (b). The intensity histogram of two nanocluster particles (line in 3a) indicates that they are 3 nm in diameter at full-width, half-maximum (c).

alloyed 12YWT steel is stable in size and composition at extremely high temperatures of 1300ºC. Results were obtained showing the unique structure and composition of the nanoclusters. Based on the physical characteristics of the nanoclusters, their remarkable stability in iron cannotbe explained by current theories in materials science. We also achieved the objective of integrating theory and modeling with experiment to develop the understanding of nanocluster formation in iron alloys. A model based on forst-principles theory was developed showing that the formaiton of nanoclusters requires enhanced oxygen solubility in iron and that this can be achieved by Ti and Y additions and on vacancies in iron. Ball milling of the pre-alloyed iron powders produces favorable conditions for enhancing the oxygen solubility and reduces the particle size of Y_2O_3, forcing it into a nonequilibrium suspension in the iron matrix. Finally, the nanoclusters form by precipitating from the iron matrix during consolidation of the ball milled powders. However, it was discovered that a low consolidation temperature, where long-range diffusion of Ti and Y atoms is negligible, resulted in the formation of nanoclusters. The results of this investigation provide a new approach to dramatically improving the high-temperature strength of iron-based alloys by dispersion of a high-number density of nanoclusters.

The results of this project showing the improved creep strength of the 12YWT and the stability of the nanoclusters at high temperature led to a collaboration with research scientists from the French Commissariat al' Energie Atomique (CEA) that resulted in a successful proposal to the International Nuclear Energy Research Initiative (I-NERI), Office of Nuclear Energy for $1.2M over three years. This project will study the deformation and fracture modes, corrosion behavior, and stability of oxide- and nanoclusters-dispersion strengthened steels under long-term high-temperature aging and understand the effects of displacement damage on the stability of nanoclusters and oxide particles using multi-MeV heavy ions.

There is growing interest in the nanocluster dispersion strengthened steels for development of advanced nuclear technologies embodied in the overall concept of Generation IV reactors and in several DOE Fossil Energy Vision 21 programs for extreme high-temperature materials for use in ultra-super-critical steam power plants.

Our effort on this project has recently stimulated a Basic Energy Science (BES) proposal entitled, "Self-Assembly of Stable Nanoclusters in Metallic Matrices," which is being led by C. T. Liu in ORNL's Metals and Ceramics Division. This proposal, which requests $3M for three years, focuses on fundamental issues of the formation mechanism and thermal stability of stable nanoclusters, including atomic-scale characterization using advanced analytical techniques; theoretical modeling by ab initio calculations and kinetic Monte Carlo simulations; and experimental studies of nanocluster formation and thermal stability applying physical metallurgy analysis, alloying designs, etc. The proposed study would also investigate hardening mechanism at ambient and elevated temperatures including atomic-scale resolution of dislocation line curvature.

References

[1]C. Suryanarayana, *Progress in Materials Science* **46**, 1 (2001).

[2]D.J. Larson, P.J. Maziasz, I-S. Kim, and K. Miyahara, *Scripta Mater.* **44**, 359 (2001).

[3]M.K. Miller, in *Atom Probe Tomography: Analysis at the Atomic Level*, Kluwer Academic Publishers Group, 2000.

[4]Swisher and Turkdogan, *Trans. Met. Soc. AIME* **239**, 426 (1967).

Combined Neutron and X-Ray Diffraction

J. W. L. Pang
Metals and Ceramics Division

The goal of this project was to demonstrate how neutron and synchrotron X-ray microbeam diffraction can be combined for the investigation of deformation mechanisms over different length scales. A series of in situ and ex situ experiments on pure Ni samples have been carried out using both techniques. Experiments designed to investigate the dependence of deformation on grain size highlighted the distinctive strengths of various X-ray and neutron techniques and illustrated how they can be applied to the study of deformation. Inhomogeneous developments of strain and rotational behaviors are found on both the micro and meso scale. Differences in the observed behavior between samples provides direct experimental evidence of grain-size and grain-boundary effects on deformation and the need to use neutron and X-ray diffraction to advance our understanding of deformation mechanisms.

Introduction

A sophisticated understanding of plastic deformation is required to predict materials behavior in service and to accelerate the development of novel new materials. For example, grain size, preferred orientation, residual stress and a host of other properties result from inhomogeneous plastic deformation. Theoretical progress in deformation modeling has been rapidly moving forward over the last two decades. Deformation is length-scale sensitive, and what is needed for comparison with theoretical models is a way to study deformation of polycrystalline materials that focuses on the three-dimensional (3-D) microscopic and mesoscopic carriers of deformation, namely, grain conglomerates, grains, subgrains, dislocation cells, and second-phase particles. A synergistic combination of techniques that cover the appropriate length scales will have a significant impact on our basic understanding of deformation and will guide the development of computational intensive models. This project focused on the exploitation of novel neutron and X-ray diffraction techniques to provide unprecedented experimental information to guide and test advanced models.

Technical Approach

There are numerous microscopic variables which affect deformation behavior. In our study, we examined the grain-size dependence of deformation. Our experimental approach was based on linking materials physics over the very different numbers of grains, and the radically different length scales that can be probed by the various 3-D techniques. Neutron penetration depths, for most elements, are on the order of centimeters, and volume-averaged internal strains in the bulk can be measured non-destructively. The sensitivity of neutron diffraction to microstrain (intergranular strain) and the application of neutron diffraction to study deformation was proven in the last decade.[1–2]

The recent development of polychromatic X-ray microdiffraction with submicron spatial resolution has revolutionized the measurement of mesoscopic structure. Individual grains, their substructures, and grain boundaries can all be studied nondestructively and in three dimensions based on white beam Laue technique.[3–4] Detailed boundary conditions and variation of deformation within a grain and across grain boundaries can be determined, which was not possible before.

Our strategy is to use neutron powder measurements to understand the statistical behavior of bulk polycrystalline grains. Based on the guidance from neutron powder measurements, X-ray microbeam Laue measurements are applied to study specific deformation features with subgrain resolution. Our experimental efforts demonstrated how these techniques can be applied to study length-scale-sensitive materials problems.

The material chosen was 99.97% pure nickel (Ni-270); this material has much reduced effects of impurity and precipitate particles compared to most alloys. The samples were fully dense, and porosity was not an issue. Two sets of samples of grain sizes 20 µm and 200 µm were prepared. A coupon from a Ni-270 extruded rod was first subjected to 5% reduction by cross rolling. The 20-µm grain size was produced by annealing at 550°C for 2 hours; 200-µm grain size was achieved by an additional annealing at 1200°C for 2 hours. Uniaxial tests were performed on both sets of samples and the evolution of microstrain, and texture was measured at various levels of plastic deformation.

The first measurements were on the 99.97% pure Ni tensile sample with 200-µm grains. The sample was

mechanically polished followed by electropolishing. Microbeam Laue measurements were carried out on the beamline ID-34E at the Advanced Photon Source, Argonne National Laboratory. Figure1(a) illustrates the experimental setup. The sample was probed by a polychromatic X-ray beam with an energy range of ~8–25 keV. Depth resolution was achieved using the differential aperture microscopy method developed by Larson et al.[4] The volumetric resolution of the measurements is 0.5(W) × 0.5 (H) × 1.0 (D) μm^3, and Laue images were collected down to 30 µm beneath the surface. After the near-surface grain pattern was measured, a 3-D grid of 5 × 5 × 30 volume elements was collected.

Measurements focused on three grains joined by a common triple junction. The local orientations along 25 lines through the sample were probed. The 5 × 5 transverse grid of the measurements are indicated in Fig. 1(b). Local orientations along the lines into the sample were probed at various plastic strains. After each deformation step, the positions of the measurements were referenced back to the triple junction, which could be located to within ±1 µm. Because the measurements resolve volumes within neighboring grains, effects of sample heterogeneity can be correlated to local deformation. Orientations are determined with a precision of <0.02° at 0% strain, comparing to ~1° for orientation imaging microscopy. As strain increases, dislocation density increases and the angular resolution drops to ~0.2° at 14% strain. The data acquisition time required for each line scan was about 20 minutes. Experiments that demand submicron resolution such as grain boundary studies and stringent angular resolution measurements can now be performed. The main drawback at present is the relatively slow count rate for depth-resolved measurements; it is not practical to conduct an extensive depth-resolved study on a large cross-sectional area. The strain resolution was determined by performing in situ loading measurements using a monochromatic beam on another Ni tensile sample. The uncertainty of the elastic stress tensor for measurements within the elastic regime was found to be ~1 part in 10^4.

Neutron diffraction measurements were carried out on the spectrometer E3 at the NRU Reactor, Chalk River Laboratories, Canada. The experimental setup is shown in Fig. 2. Uniaxial tension was applied to samples with grain sizes of 20 µm and 200 µm. The accumulated strains and texture changes within the grains over the sampling volume were then measured as a function of (*hkl*) reflections and sample orientations with respect to the tensile axis. Measurements were performed on all the undeformed samples to ensure accurate determination of strain and texture evolution introduced by the applied tension instead of any previous processing procedures. The neutron scattering factor for Ni is large, and fast data acquisition with high precision was achieved.

Knowledge of the variations in strains and misorientations at the subgrain level is essential to complement neutron diffraction measurements where an ensemble average is probed. It is important to note however that deformation studies on many bulk polycrystals are difficult or impossible with x-ray microbeams, because

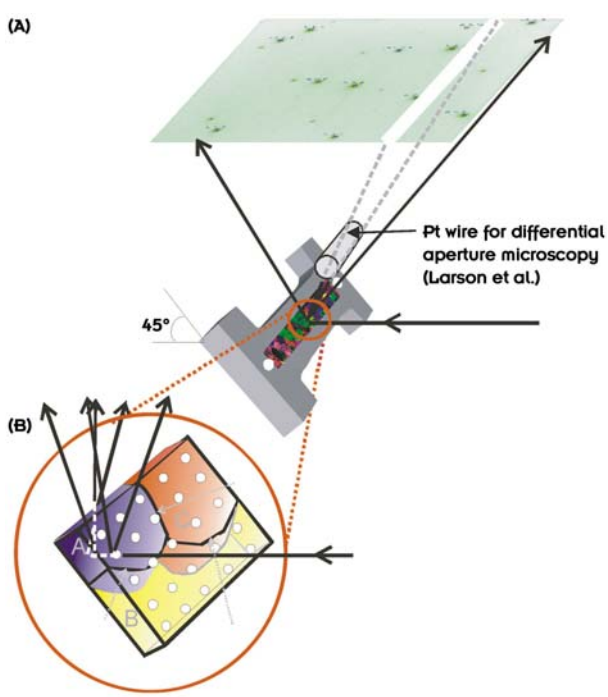

Fig. 1. (a) Schematic of the experimental setup of the measurements on beamline ID-34E; (b) the three grains on which the measurements were focused on.

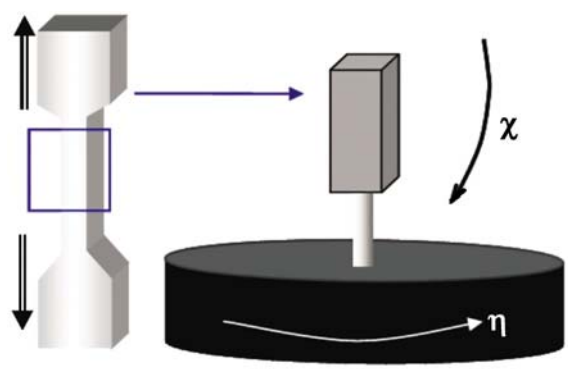

Fig. 2. The tensile sample was put on an Eulerian cradle for the neutron diffraction measurements on E3 at the NRU Reactor. Information on the intergranular strain variations as a function of angular positions were determined by measuring over a quadrant of a hemisphere on a (15°, 15°) grid.

of the relatively short penetration depth (50 µm for Ni). In order to make measurements with submicron resolution, the deformed samples were cut by electron discharge along the tensile axes to produce samples ~200 µm thick. The samples were then mechanically ground and chemically etched to reduce the thickness down to ~50 µm. Selective regions of the samples were then measured by X-ray microbeam, as described above.

Results and Accomplishments

The average flowcurves of the 20-µm and 200-µm grain-sized samples are plotted in Fig. 3. The yield stress of the fine grained samples is 60% greater, and the hardening behavior is almost identical for both samples. Large residual tensile strains were found by neutron diffraction for the (002) reflection along the tensile axis for both grain sizes. Residual strains for other reflections are within 0.03% in all measured sample directions. The significant observation is the difference in strain magnitudes between the two grain sizes. Figure 4 shows the maximum amplitudes of the residual strains for (002) at plastic strain of 0.3, 1, 5, and 15%. Samples with larger grain size consistently show smaller lattice strains. It was found that the lattice strains for the large-grained samples reached to plateau at around 5% plastic strain, whereas lattice strains continue to increase for the 20-µm grain samples.

Texture evolution from 0% to 15% strain was determined, and the difference between the two sets of samples was small. However it is believed that the difference will be more significant when rotational incompatibility among grains increases with deformation. These results show convincingly that, with well-designed experiments, neutron diffraction can be used to study the effects of microstrucutral parameters on deformation and well-characterized samples.

A self-consistent (SC) model[5] has been applied to simulate the deformation process. The input parameters were obtained from the macroscopic flow curves (Fig. 3). The predicted strain magnitudes are compared to the experimental results in Fig. 4. Because the SC model is not length-scale sensitive, the model can only capture the effects introduced by yield-strength differences. The results clearly show that the model overestimates the strain magnitudes and cannot capture the differences observed between the grain sizes.

Residual strain profiles across a twin boundary and a high-angle boundary in the 50-µm-thick slices cut out from the 1% deformed samples were measured by microbeam Laue diffraction and the results are shown in Fig. 5. These measurements clearly indicate variations in strains across grain boundaries. The important observation is the strain discontinuity observed in the high-angle boundaries but not the twin boundaries for both grain sizes. It was also

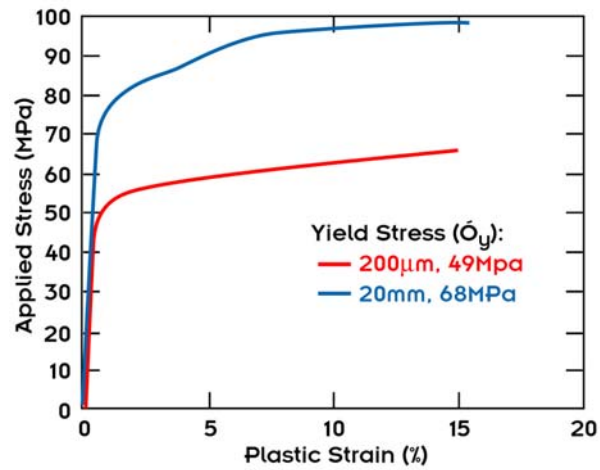

Fig. 3. The flowcurves for the Ni-270 samples of grain sizes 20 µm and 200 µm.

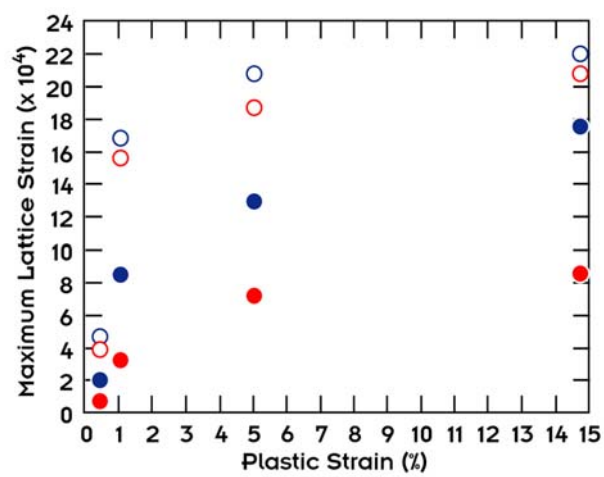

Fig. 4. Maximum lattice strain for reflection (002) determined by neutron diffraction as a function of plastic deformation. Predictions determined by SC model are plotted together with the experimental data.

found that the strain gradients across the boundaries are sharper in the large-grained sample. More measurements will be needed to develop statistically significant results. However the results thus far provide direct submicron evidence to validate the general belief that grain boundary behavior is a function of grain size and is dependent on the grain boundary types. Companion misorientation measurements were made, and similar discontinuities across grain boundaries were found for the high-angle grain boundaries.

These experimental results will be used to test a length-scale-sensitive deformation model which is based on crystal plasticity with finite element discretization.[6] If the assumptions in the model are correct, the model should capture both the microscopic and mesoscopic information from the experiments.

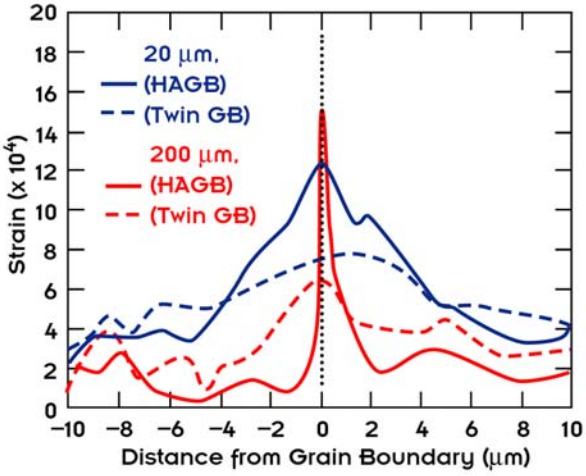

Fig. 5. Lattice strains in the loading direction across grain boundaries for 1% deformed samples. HAGB indicates high-angle grain boundaries.

Summary and Conclusions

This project demonstrates the complementary capabilities of neutron diffraction and X-ray microbeam Laue techniques in the study of deformation mechanisms. A synergistic combination of these techniques can provide experimental information which will make significant contribution to the understanding of deformation mechanisms and ultimately advance our ability to predict materials performance.

For the last two years, there has been a continuing emphasis on the promotion of the use of neutron for materials research in the anticipation of the completion of the Spallation Neutron Source (SNS) in 2006. This project was designed to use neutron scattering, our strong in-house capability in advanced materials characterization, and world-leading expertise in microbeam Laue technique to examine deformation. Another core competency at ORNL is parallel computing. ORNL has an active community in parallel processing and recently was selected to host the next-generation parallel processing machine designed to return computational preeminence to the United States. Computer-intensive modeling efforts are under way. This research and emerging new computational tools place ORNL in a unique position to advance deformation modeling.

This project is relevant to DOE's Basic Energy Science program to which a follow-on proposal has been submitted. It will provide unique insights into the deformation behavior of polycrystalline materials, which is one of the major considerations in the development of new structural materials. The length scale of the results will be of direct relevance to many developing deformation models.

References

[1]T. M. Holden, R. A. Holt, and J. W. L. Pang, "Intergranular stresses in ZIRCALOY-2," *Metallurgical and Materials Transactions a-Physical Metallurgy and Materials Science* **33**(3), 749–755 (2002).

[2]J. W. L. Pang et al., "The generation of intergranular strains in 309H stainless steel under uniaxial loading," *Acta Materialia* **48**(5), 1131–1140 (2000).

[3]R. I. Barabash et al., "Application of white x-ray microbeams for the analysis of dislocation structures," *Review of Scientific Instruments* **73**(3), 1652–1654 (2002).

[4]B. C. Larson et al., "Three-Dimensional X-ray Structural Microscopy with Submicrometre Resolution," *Nature* **415**(6874), 887–890 (2002).

[5]P. A. Turner and C. N. Tome, "A Study of Residual-Stresses in Zircaloy-2 with Rod Texture," *Acta Metallurgica Et Materialia* **42**(12), 4143–4153 (1994).

[6]G. B. Sarma and P. R. Dawson, "Effects of interactions among crystals on the inhomogeneous deformations of polycrystals," *Acta Materialia* **44**(5), 1937–1953 (1996).

Electrical Conductivity at the Nanoscale

A. P. Baddorf,[1] C. L. Fu,[2] S. V. Kalinin,[1] J. Shen,[1] H. H. Weitering,[1,3] J. F. Wendelken,[1] and X. Zhang[4]
[1]*Condensed Matter Sciences Division*
[2]*Metals and Ceramics Division*
[3]*The University of Tennessee*
[4]*Computer Science and Mathematics Division*

This research focused on measurement and calculation of conductivity in nanoscale objects, specifically objects made with transition metal oxides. Nanoscale transition metal oxides are complex because the structural, electronic, and magnetic properties are strongly coupled, but not always linearly. The result is ferroelectric, superconducting, and magnetoresistive materials with great potential as optical switches, magnetic sensors, and transducers where properties can be "tuned" by the introduction of reduced dimensions, doping, or strain. This project focused on low-dimensional systems of ruthenium oxides, with their metal-insulator switching properties, and on manganese oxides, with potential applications for their colossal magnetoresistance. The goal was to both understand transport in these systems and to develop the tools to more generally study electrical conductivity at the nanoscale.

Introduction

Electronic transport in nanoscale materials, such as ultra thin films, interfaces, or surfaces, challenges our understanding of the mechanisms of conductivity. In reduced dimensions, quantum interference of scattered electrons gains importance and nanoscale films, interfaces, or surfaces can exhibit qualitatively different transport from bulk materials. One exciting class of materials receiving increasing attention is the transition metal oxides, which display a fascinating and complex interaction between atoms, electrons, and spins, to a degree unseen in any other materials. Many are highly correlated electron systems that possess several competing quantum mechanical ground states. This competition often makes these materials "bad metals" but also produces a number of highly useful physical phenomena, including superconductivity, colossal magnetoresistance, and ferroelectricity. Electrical transport properties are especially intriguing as they can be tuned over many orders of magnitude by small changes in composition, temperature, strain, or by application of an external magnetic field. This sensitivity makes transition metal oxides excellent candidates for sensors and switches. Technological applications of these materials requires a greater insight into their mechanisms and the development of tools, both experimental and theoretical, for their study.

Technical Approach

This proposal sought novel approaches to measuring and calculating electronic transport of transition metal oxides in low dimensions (i.e., surfaces, thin films, or wires). Where possible, these measurements were made in ultra high vacuum conditions. This involved either growing thin films and measuring in situ, or cleaving bulk samples in vacuum. The growth and characterization of these materials involved an array of tools, including pulsed laser deposition (PLD) growth, low energy electron diffraction (LEED) and scanning tunneling microscopy (STM) for structure, and X-ray photoemission (XPS) and Auger electron spectroscopy (AES) for chemical composition.

Our experimental plan incorporated four approaches to conductivity measurements. The first is most direct: a macroscopic four-point probe with probe spacing around 100 mm. The second approach was to use a microscopic four-point probes develop at the Technical University of Denmark. The third approach is was to apply scanning probe microscopy (SPM) both to obtain local spectroscopy measurements with nanometer resolutions and to use the probe tip as a local voltage probe. Part way through the project, we added a fourth experimental tool, reflection electron energy loss spectroscopy (EELS) with advantages for a specific system discussed below.

The theoretical objective of this project was to model the electron transport properties in order to understand the underlying mechanisms and to explain and suggest future measurements. First-principles methodology was employed, since this approach provides the deepest insight into the fundamental physics and the greatest information on the transport mechanisms. The approach involved a two-step process. First, the ground-state electronic

structure in the film or surface was calculated, since electron transport is inherently linked to the availability and mobility of electrons near the Fermi energy. Electronic structure results were subsequently employed as input for transport calculations.

Results and Accomplishments

Our research has discovered nanoscale effects on conductivity in three types of transition metal oxide systems. The first was evidence that the charge induced by polarization of a ferroelectric material can lead to a metallic surface on the insulating substrate. First-principles local-density-functional calculations for the electronic structure of a film of $BaTiO_3$ show that Ti-3*d*- and O-2*p*-related surface states are present. In the cubic phase, the O surface states are fully occupied and the Ti surface states are fully empty, resulting in an insulating surface. When the bulk material is polarized into the tetragonal state (either by changes in temperature or electric field), the O surface states on one face of the film supply electrons to the Ti surface states on the opposite face. The result is, while the bulk remains insulating, both faces of the film become conducting: on one face through the O surface states, and on the other through the Ti surface states. This is illustrated in Fig. 1, which shows the density of states on O and Ti in the bulk and at the two surfaces.[1] This result could lead to development of highly sensitive thermal and electric field sensors.

A second area of success has been the establishment of experimental capabilities for in situ growth and measurement of conductivity in transition metal oxides that exhibit colossal magnetoresistance. Colossal magnetoresistance (CMR) is a very large change in conductivity in a magnetic field and may replace giant magnetoresistance materials now used in virtually all hard disk drives. Combining pulsed laser deposition with concurrent electron diffraction, we have grown ultra thin, single-crystal films of manganese oxides on insulating $SrTiO_3$. In one example, the effects of strain and nanoscale confinement on the magnetic and resistivity transition temperatures for dimensions down to 7 nm have been measured for $La_{0.7}Sr_{0.3}MnO_3$ films. Results are shown in Fig. 2.

The strong spin-charge-lattice interaction in manganites often leads to a striking phenomenon called electronic phase separation, which indicates the coexistence of a range of exotic electronic and magnetic phases despite the single-crystal structure.[2] The role of electronic phase separation in the related physical properties such as CMR is a hotly debated issue in the field of condensed matter physics.

Using in situ scanning tunneling microscopy/spectroscopy, we have observed both large-scale (greater than a few tens nanometers) and nanoscale electronic phase

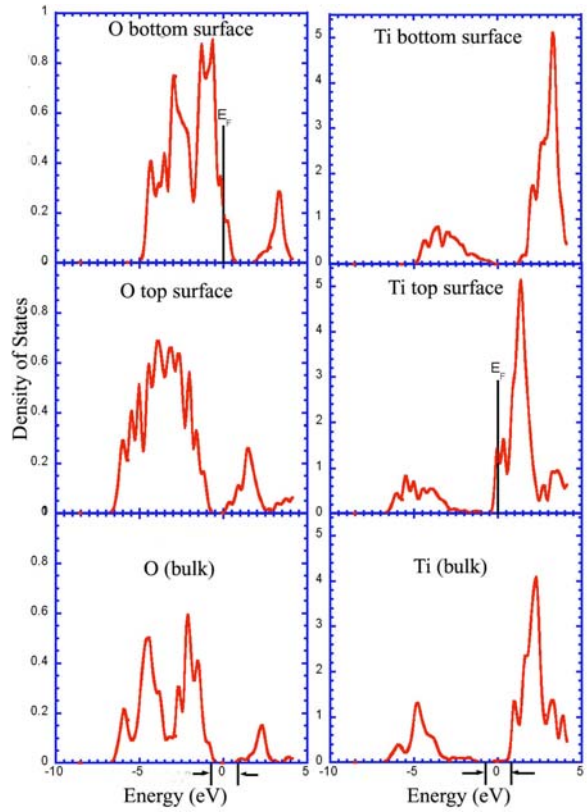

Fig. 1. First principles calculation of the layer-projected density of electronic states of O and Ti atoms in a ferroelectric $BaTiO_3$ slab. The ferroelectric distortion toward the top surface breaks the symmetry and the polarization adds electron density into conducting surface

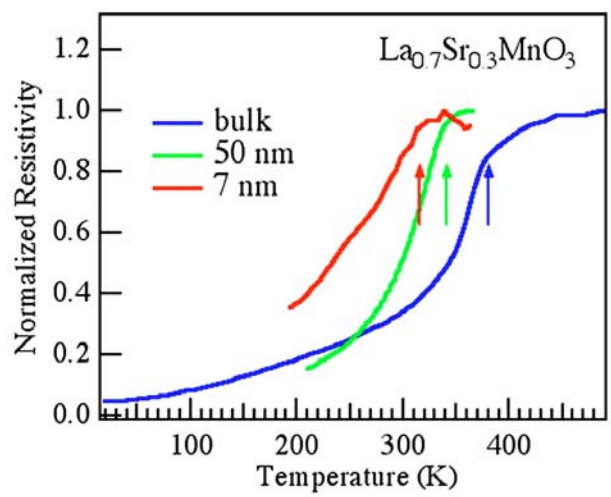

Fig. 2. In situ measurements of the resistivity of $LaCaMnO_3$ films grown using pulsed laser deposition show the metal-insulator transition decreases for thinner films. This is correlated with a decrease in the magnetic phase transition in the same films and reveals the results of strain and confinement.

separation in epitaxially grown thin films of $(La_{5/8-0.3}Pr_{0.3})Ca_{3/8}MnO_3$.[3] Images in Fig. 3 show that the topography (a) is relatively featureless, but the conductivity map (b) varies considerably across the same region. The bottom panel (c) illustrates the different metallic and insulating characteristics in the different regions. While the large phase separation domains are present only below the Curie temperature, the nanoscale phase separation clusters exist at temperatures both below and above the Curie temperature, which implies that the small clusters may originate from doping-related disorder. This is consistent with theories showing that quenched disorder is the driving force for the appearance of large-scale phase separation in magnates.[4]

A third type of nanoscale transition metal oxide system studied in this project is the surface of ruthenates. Sr_2RuO_4 is a superconducting relative of the high-T_c copper oxides, but the isoelectronic material Ca_2RuO_4 is insulating. By examining compounds of the alloy $Sr_xCa_{1-x}RuO_4$, a temperature-dependent metal-insulator transition is observed. In particular, $Ca_{1.9}Sr_{0.1}RuO_4$ exhibits a Mott transition below 154 K in bulk single crystals.[5] Using electron energy loss spectroscopy, which is sensitive only to the surface, we have been able to distinguish the transition at the surface from that of the bulk material. The surface has a surprisingly lower metal-insulator transition temperature ~130 K (Fig. 4). The lowering of transition temperature is intimately related to different lattice distortions at the surface (a relatively smaller orthorhombic distortion but larger RuO_6 compression than in the bulk), indicating a strong electron-phonon coupling in addition to electron-electron correlation. These results imply a coexistence of a metallic surface on a nonmetallic bulk.

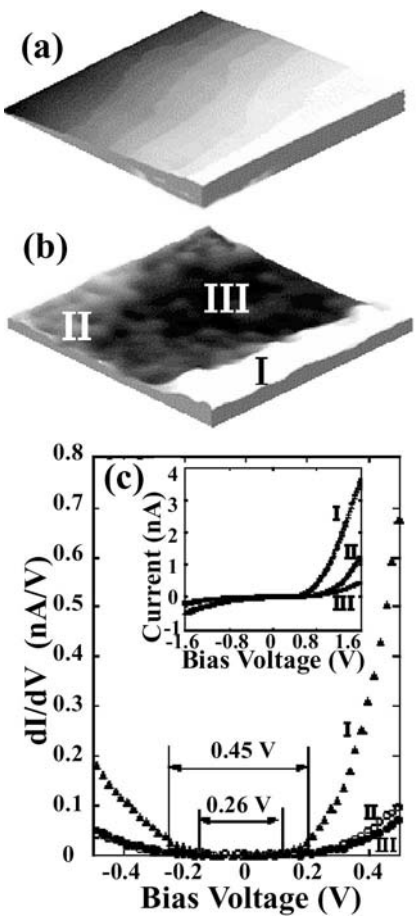

Fig.3. 240 nm × 240 nm topography image (a) and corresponding current image (b) obtained simultaneously from an in situ–grown $(La_{5/8-0.3}Pr_{0.3})Ca_{3/8}MnO_3$ film at T = 60 K. The current image is shown for a voltage bias of 1.6 V. (c) Derivative dI/dV vs V curves obtained from three different areas marked as I, II, and III. The inset shows corresponding I/V curves. The variation in these curves reveals different conductivity characteristics within the film caused by nanophase electronic separation.

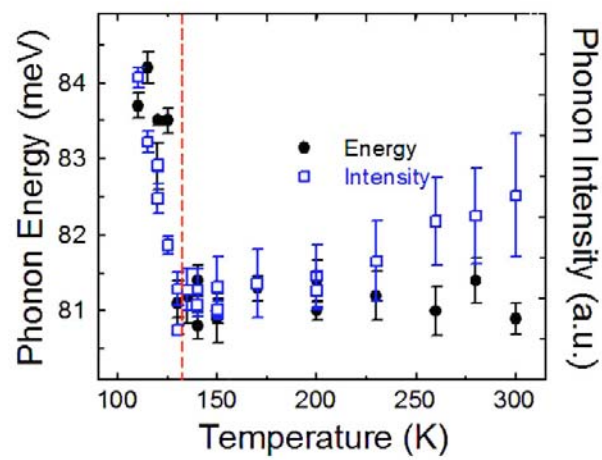

Fig. 4. Electron energy loss spectra reveal a surface Mott transition at ~130 K, lower than the bulk transition temperature of 154 K. The transition is reflected in the phonon energies (left axis) and intensities (right axis).

Summary and Conclusions

Transition metal oxides continue to show a number of novel electrical conductivity phenomena, particularly at dimensions confined to the nanoscale. We have observed a number of metal-insulator transitions on the surface of a ferroelectric, $BaTiO_3$, where the bulk remains insulating, and on the surface of a ruthenate, $Ca_{1.9}Sr_{0.1}RuO_4$, where the bulk becomes an insulator at higher temperatures than the surface. These materials should be pursued as the basis for sensor devices since the strong metal-insulator transition is readily interfaced to electronic devices.

We have also provided a great step toward understanding and controlling electronic transport in colossal magnetoresistance materials. Direct identification of electronic phase separation in $(La_{5/8-0.3}Pr_{0.3})Ca_{3/8}MnO_3$

can identify the mechanism behind colossal magnetoresistance and lead to applications such as hard drive read heads.

More generally, we have developed techniques and expertise for measuring electrical transport in nanoscale materials, using both direct electrical contacts and by analysis of energy losses in scattered electrons. This project has also advanced calculational capabilities, applying first-principles theory to a class of materials, ferroelectrics, which has previously been elusive. In developing these techniques, we have established collaborations with world-recognized leaders in the field of nanoscale conductivity, including Andy Millis, University of Columbia, Allan MacDonald, University of Texas, and S. Kalinin, now a Wigner fellow at ORNL. These techniques and collaborations promise to be of great benefit to future research, to development of the Center for Nanoscale Materials Science at ORNL, and to the interests of the Defense Advanced Research Projects Agency's Defense Sciences Office.

References

[1]M. Krcmar and C. L. Fu, "Structural and electronic properties of $BaTiO_3$ slabs: Mechanism for surface conduction," *Phys. Rev. B* **68**, (2003) 115404.

[2]N. Mathur and P. Littlewood, "Mesoscopic Texture in Manganites," *Phys. Today* **56**, 25 (2003).

[3]J. X. Ma, Z. Gai, M.A. Torija, E. W. Plummer, and J. Shen, "Observation of Two Length Scales for Phase Separation in $(La_{5/8-0.3}Pr_{0.3})Ca_{3/8}MnO_3$," submitted to *Phys. Rev. Lett*. (2003).

[4]A. Moreo, M. Mayr, A. Feiguin, S. Yunoki, and E. Dagotto, "Giant Cluster Coexistence in Doped Manganites and Other Compounds," *Phys. Rev. Lett.* **84**, 5568 (2000).

[5]S. Nakatsuji and Y. Maeno1, "Quasi-Two-Dimensional Mott Transition System $Ca_{2-x}Sr_xRuO_4$," *Phys. Rev. Lett.* **84**, 2666 (2000).

Self-Organized Copolymer and Nanoporous Oxide Thin-Film Templates for Controlled Synthesis and Periodic Replication of Nanoscale Materials

S. Dai,[1] Z. W. Pan,[1] D. B. Beach,[1] M. Dadmun,[2] D. H. Lowndes,[3] V. I. Merkulov,[4] S. J. Pennycook,[3] and C. Tsouris[5]

[1]*Chemical Sciences Division*
[2]*Deparment of Chemistry, University of Tennessee*
[3]*Condensed Matter Sciences Division*
[4]*Engineering Science and Technology Division*
[5]*Nuclear Science and Technology Division*

This project focused on (1) the use of ordered mesoporous oxide thin film with controlled orientations and locations to synthesize well-aligned arrays of one-dimensional (1-D) nanostructures and (2) the development of new synthetic techniques to rationally synthesize 1-D nanostructures. The project demonstrated that highly aligned arrays of multi-wall carbon nanotubes could be grown in a high yield on sol-gel-prepared mesoporous silica film doped with iron nanoparticles. By combination of the sol-gel and shadow-mask techniques, a simple and low-cost methodology was developed to grow micropatterns of aligned carbon nanotube towers. In addition, single-crystalline quasi-aligned germanium nanowires were grown on the sol-gel-prepared silica film doped with gold nanoparticles. This project also demonstrated that molten gallium could be used as an efficient catalyst for the growth of 1-D nanomaterials. For example, carbon nanotubes with large inner/outer diameter ratio were first synthesized by using gallium as the catalyst. Complex SiO_x nanowire assemblies with a variety of morphologies were synthesized by using gallium as the catalyst and SiO powder and SiH_4 gas as the source materials. The gallium-catalyzed nanowire growth exhibits many interesting new nanowire growth phenomena that enrich current nanowire growth mechanism.

Introduction

One-dimensional (1-D) nanostructures have attracted much attention in the past decade because of their unique electrical, magnetic, optical, and mechanical properties, as well as their potential applications.[1] The key to developing advanced 1-D nanostructure-based nanodevices is the efficient synthesis of nanostructures with controlled size distribution, growth direction, and morphology. Thus, controlled growth of 1-D nanostructures is essential for both basic research and technical applications. One objective of this project is to develop a novel methodology for using ordered mesoporous oxide as generic nanoscale reactors for manufacturing and replicating technologically important 1-D nanostructures, for example, aligned carbon nanotubes and semiconductor nanowires. The other objective of this project is to develop a new synthetic route for rationally growing new kinds of 1-D nanostructures that are difficult to be synthesized by traditional methodologies.

Technical Approach

(a) Vertically aligned carbon nanotubes and their patterns grown on sol-gel-prepared mesoporous silica film doped with iron nanoparticles

We have successfully synthesized highly aligned arrays of multi-wall carbon nanotubes on iron-doped mesoporous silica thin films by chemical vapor deposition (CVD). The silica films were prepared by a sol-gel method coupled with surfactant or block copolymer template synthesis. Two kinds of solution, Solution I and Solution II, were used for preparation of the silica films. Solution I was prepared by mixing tetraethoxysilane (TEOS, 3 mL), $Fe(NO_3)_3$ aqueous solution (1.5 *M*, 3 mL), and ethanol (10 mL) by means of magnetic stirring for 1 h. For Solution II, 0.8 g of Pluronic P-123 triblock copolymer was added into Solution I to increases the viscosity of the solution, which facilitates the formation of a very thin and uniform film on silicon wafer without cracking.

Two kinds of film-like iron/silica substrates were prepared for nanotube growth: (1) thick film (with thickness of ~30 to 50 μm) without patterning and (2) thin film (with thickness of ~ 1 μm) patterned with transmission electron microscope (TEM) grids. For the nonpatterned thick film, the solution was dropped onto the surface of a

silicon wafer to form a film of solution with a thickness of about 30 to 50 μm. After gelation, the gel was dried overnight at 80°C to remove the excess water and solvent, during which time the film cracked into small pieces and detached from the wafer surface to form film-like freestanding substrates.

For the patterned thin film, the solution was coated on silicon wafers by dip coating to form a very thin film of solution. When the film was still in the liquid state, copper or gold transmission electron microscope (TEM) grids with square, hexagon, or other kinds of openings were placed on the film to act as a shadow mask. During the process of gelation, Solution I tended to break down in each opening of the TEM grid because of the development of holes in the film, resulting in the formation of a ring-like solid catalyst film along the edge of each opening [Fig. 1(a)]. For Solution II, however, a stable and uniform solid film was formed in each hole of the grid after gelation [Fig. 1(c)], due to the effect of triblock copolymer. These two kinds of catalyst film configurations will result in the formation of two kinds of micropatterns of nanotube towers, that is, solid towers [Fig. 1(d)] for the uniform film and hollow towers [Fig. 1(b)] for the ring-like film. In addition, our results show that the morphologies of the nanotube patterns can be easily controlled by using TEM grids with different openings and by tuning the parameters in preparing the patterned substrates.

Both kinds of substrates were then loaded into a tube furnace and calcinated at 450°C for 10 h under vacuum condition, followed by reduction at 600°C for 5 h in hydrogen atmosphere. At this stage, large quantities of iron/silica nanoparticles formed on the film surfaces due

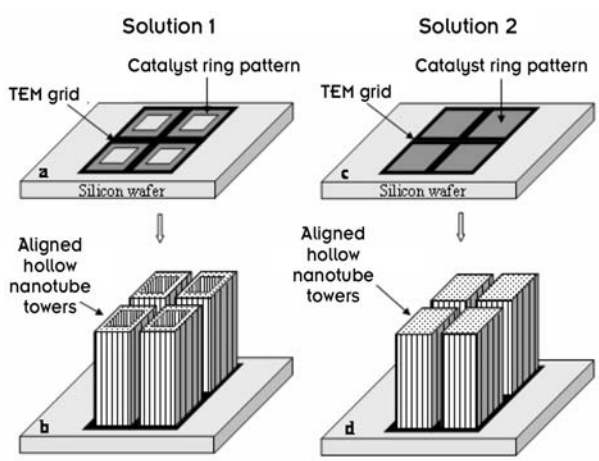

Fig. 1. Schematic diagram of the ring-like (a) and uniform film-like (c) catalyst patterns formed inside the TEM grids with square openings by using Solution I and Solution II as the catalyst precursors, respectively. The ring-like catalyst pattern results in the formation of micropattern of hollow tube towers (b), while the uniform film-like catalyst pattern generates micropattern of solid tube towers (d).

to the transportation of Fe species from within bulk substrate and subsequent aggregation, acting as catalysts for nanotube growth. Finally, acetylene (10 sccm) was introduced into the reaction chamber and aligned and/or patterned nanotubes were grown on the substrates at 700°C for 1 to 5 h.

(b) Single-crystalline quasi-aligned germanium nanowires grown on sol-gel-prepared mesoporous silica film doped with gold nanoparticles

The above mentioned sol-gel technique can be adapted to prepare silica film doped with gold nanoparticles for growing Ge nanowires by substituting $HAuCl_4$ for $Fe(NO_3)_3$. The procedure for substrate preparation is similar to that described above. Prior to being loaded into furnace for nanowires growth, the substrates were annealed at 400°C in air for 2 h, during which time large quantities of Au nanoparticles with diameters of 50–100 nm were formed and evenly distributed on the substrate surface. These Au particles act as seeds for Ge nanowires growth. The Ge nanowires growth was then carried out in a tube furnace by heating Ge powder at 900°C under an Ar flow of 50 sccm and a pressure of 250 Torr for 10 to 60 min.

(c) Gallium-catalyzed growth of carbon nanotubes and SiO_x nanowire assemblies

The vapor-liquid-solid (VLS) crystal growth mechanism, proposed by Wagner and Ellis in 1964 for Si whisker growth,[2] has been widely used to guide the growth of various kinds of 1-D nanostructures including carbon nanotubes and nanowires of semiconductors and oxides. In this mechanism, a small size (5–100 nm in diameter), high-melting-point metal (such as Au and Fe) was used as the catalyst to direct the nanowires' growth direction and defines the diameter of the crystalline nanowire. In this project, we showed that a large size (up to tens of micrometers in diameter) and low-melting-point Ga droplet can be used as an effective catalyst for large-scale growth of multi-wall carbon nanotubes and aligned SiO_x nanowires. Many interesting growth phenomena were observed in our studies.

In the Ga-mediated growth of carbon nanotubes, GaN powder was used as a source of Ga and C_2H_2 was used as the carbon source. The experiment was conducted in a tube furnace at 1150°C under 200 Torr with a C_2H_2 flow rate of 10 sccm and carrier gas Ar flow rate of 50 sccm for 1 h. The carbon nanotubes were grown on the alumina substrates located at the downstream part of the furnace.

In the Ga-catalyzed SiO_x nanowires growth, GaN was also used as the Ga source, and the Si source was provided by either heating SiO powder at 1350°C (the GaN powder was put at the upstream part where the temperature is about 1150°C) or thermal pyrolysis of SiH_4 gas at 1150°C. In

both cases, the growth time is 1 h and the products were deposited at the alumina substrates located at the downstream low temperature part.

For all above syntheses, the products were characterized by scanning electron microscope (SEM), transmission electron microscope (TEM), high-resolution TEM (HRTEM), and energy-dispersive X-ray (EDX) spectroscopy.

Results and Accomplishments

(a) Vertically aligned carbon nanotubes and their patterns[3,4]

Figure 2 shows the SEM and TEM images of the aligned carbon nanotubes and nanotube patterns. For the film-like nonpatterned thick substrates, the nanotubes grow out perpendicularly from all substrate surfaces to form aligned nanotube arrays with the same density and length. This growth feature is clearly displayed in Fig. 2(a), which shows the nanotube arrays growing out perpendicularly from the four adjacent surfaces of a substrate corner. The edge of the substrate is very clear, and the angle between two adjacent arrays is about 90°. Figure 2(a) also shows that the nanotube arrays grown on different surfaces have the same length and nanotube density. High-magnification SEM examinations reveal that the nanotubes are vertical to the substrate surface and remain aligned as their length increases. The length of the nanotube arrays increases with the period of growth at a rate of ~15 μm/h. Figure 2(b) is a TEM image of a bundle of aligned nanotubes, showing that the nanotubes are of uniform diameter, with outer and inner diameters in the range of 20 to 30 nm and 5 to 10 nm, respectively. No catalyst particles were observed inside the nanotubes. HRTEM studies show that the nanotubes are well graphitized and typically consist of 10 to 30 concentric graphite layers [inset in Fig. 2(b)].

By using the patterned substrates prepared by our unique and simple combined approach, we can grow nanotube patterns with a variety of morphologies and configurations. As viewed from the top, patterned nanotube towers in the shape of squares [Fig. 2(c)], hexagons [Fig. 2(d)], letters [Figs. 2(e) and 2(f)], and Arabic numerals [Fig. 2(g)] were obtained by using the corresponding TEM grids as the shadow masks. More importantly, patterns with complex morphologies, which are difficult to achieve by other techniques, can be readily prepared by our method. For example, by using the ring-like catalyst film pattern [see Fig. 1(a)] as the substrate and the TEM grids absent during nanotube growth, a nanotube network can be formed along the trace of the TEM bars [Fig. 2(h)] which replicates the structure of the original TEM grid very well. On the other hand, if the TEM grids remained in place during carbon deposition, micropatterns of hierarchically ordered carbon tubes (i.e., ordered microtubes composed of aligned carbon nanotubes) were obtained on the ring-like catalyst film pattern [Figs. 2(i) and 2(j)]. Note that all the towers shown in Fig. 2(c–j) are composed of highly aligned carbon nanotubes, which grow perpendicularly from the substrate surface and have the microstructures as shown in Fig. 2(b).

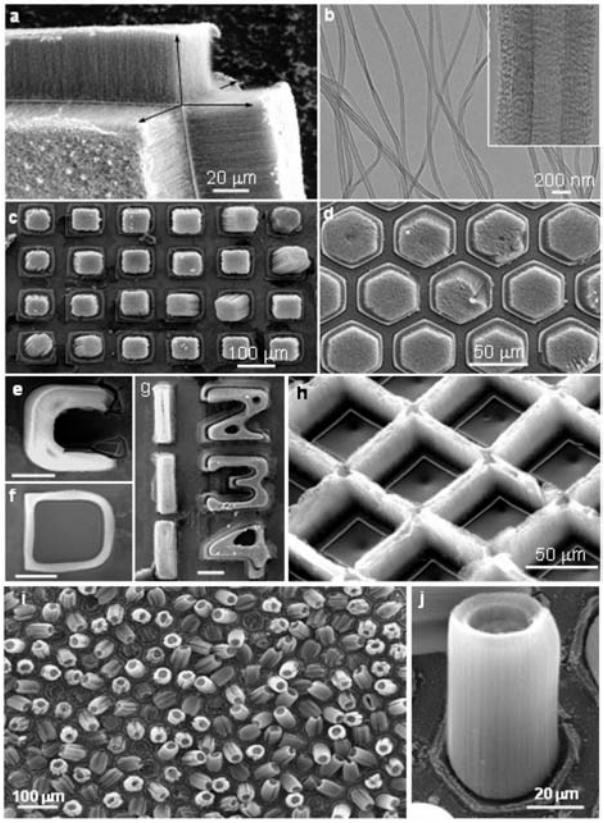

Fig. 2. SEM and TEM images of aligned carbon nanotubes and nanotube patterns. (a) A close-up view of a substrate corner, showing aligned nanotubes growing out perpendicularly from four adjacent surfaces of the corner. The growth direction of the nanotubes on each surface is indicated by a black arrow. (b) TEM image of a bundle of aligned carbon nanotubes. Inset, HRTEM image of a carbon nanotube, showing well-ordered graphitic lattice fringes. (c) Micropatterns of regularly arranged square towers obtained by using a 200 mesh copper grid as the mask after 4 h of growth. (d) Micropatterns of regularly arranged hexagonal towers obtained by using a 300 mesh copper beehive grid as the mask after 2.5 h of growth. (e) and (f) Letters consisting of vertically aligned carbon nanotubes. (g) Arabic numerals consisting of vertically aligned carbon nanotubes. Scale bar in e–g, 50 μm. The substrates corresponding to images c–g were prepared by using Solution II (with copolymer) as the catalyst precursor. (h) A nanotube network grown along a catalyst network that initially existed under the bar of a TEM grid. The grid was removed before carbon deposition. (i) Low-magnification SEM image of micropattern of hierarchically ordered carbon tube towers formed by using a 400 mesh copper beehive grid as shadow mask after 3 h of growth. (j) High-magnification image of one hierarchically ordered hollow tower. The substrates corresponding to images c–g were prepared by using Solution I (without copolymer) as the catalyst precursor.

(b) Single-crystalline quasi-aligned germanium nanowires[5]

Figure 3 shows the SEM and TEM images of Ge nanowires grown on film-like gold/silica substrates. After the growth, the substrates were covered with brown nanowire materials in a high-yield, as shown in Fig. 3(a). The nanowires are straight with length up to tens of micrometers. Similar to the growth behavior of aligned carbon nanotubes shown in Fig. 2, the Ge nanowires grown on the gold/silica substrate tend to grow perpendicularly to the substrate surface, and in some case, quasi-aligned nanowire array can be obtained [Fig. 3(b)]. The nanowires shown in Fig. 2(b) are very straight and uniform in diameter (~50–80 nm). Each nanowire is tipped with an Au nanoparticle with diameter comparable to the connected nanowire [inset in Fig. 3(b)], showing typical VLS growth feature.

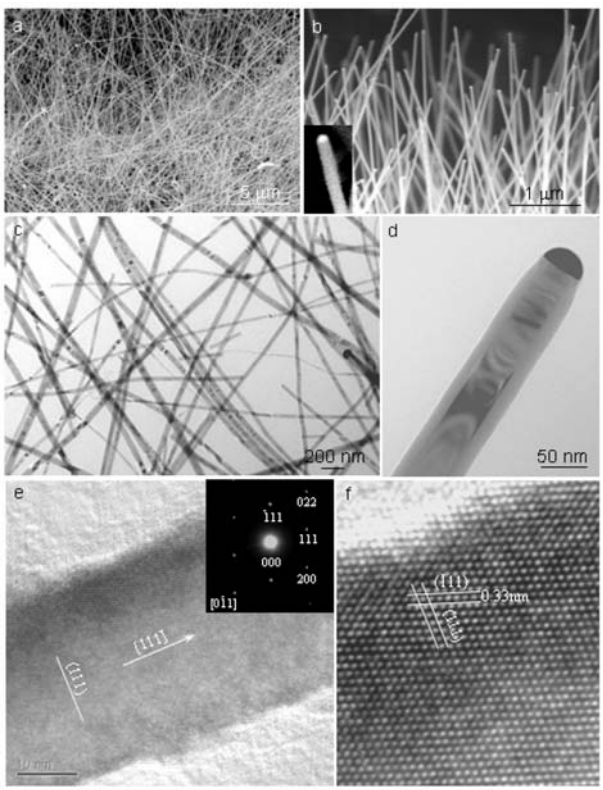

Fig. 3. SEM and TEM images of Ge nanowires grown on sol-gel prepared gold/silica substrate. (a) SEM image showing straight Ge nanowires grown in high-yield and high purity. (b) Quasi-aligned straight Ge nanowires with uniform diameter. The inset shows a nanowire tipped with an Au nanoparticle. (c) Low-magnification TEM image showing straight and uniform Ge nanowires. (d) TEM image of an individual Ge nanowire with a hemispherical Au nanoparticle located at the tip, showing a core-shell structure. (e) HRTEM image of a Ge nanowire with diameter of ~40 nm. The inset shows a corresponding electron diffraction pattern. (f) An atomic resolution image taken from the edge part of the nanowire in (e).

The uniformity of the Ge nanowires was further proved by TEM investigation. Figure 3(c) is a low-magnification TEM image of the Ge nanowires, showing straight and uniform nanowires. Figure 3(d) is a TEM image of an individual Au-tipped Ge nanowire, showing a core-shell structure. EDX analysis shows that the crystalline core is Ge and the amorphous sheath has an approximate composition of GeO_2. Figure 3(e) is a HRTEM image of a Ge nanowire with diameter of ~40 nm. The lattice fringes perpendicular to the wire axis correspond to the (111) lattice planes [spacing, 0.33 nm; see the atomic resolution image in Fig. 3(f)] of Ge, indicating a [111] growth direction. This direction was confirmed by the selected area electron diffraction pattern [inset in Fig. 3(e)] recorded perpendicular to the nanowire long axis, which could be indexed as the $\langle 0\bar{1}1 \rangle$ zone axis of crystalline Ge.

(c) Gallium-mediated growth of carbon nanotubes[6]

Figure 4 shows the SEM and TEM images of the carbon nanotubes catalyzed by molten Ga. The Ga-catalyzed nanotubes tend to grow in groups, in which hundreds of nanotubes radially grow upward around an island with a diameter of ~10 µm, as shown in Fig. 4(a). High-magnification SEM observations and EDX analyses

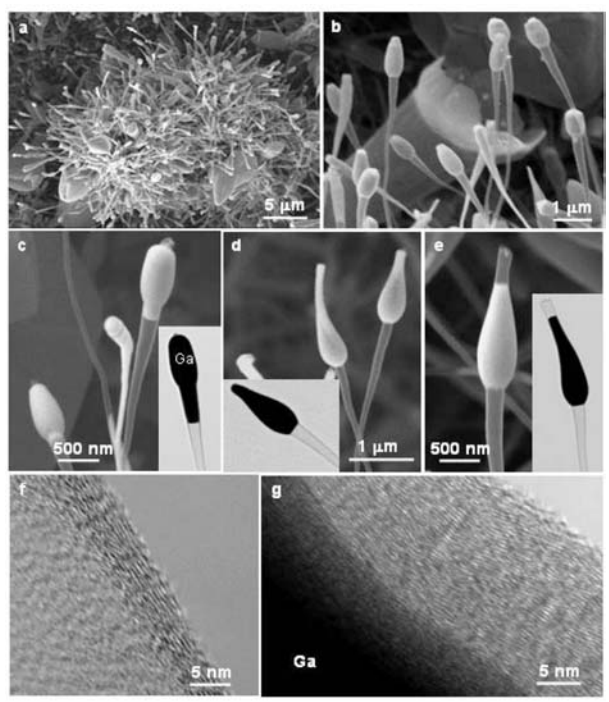

Fig. 4. SEM and TEM images of Ga-mediated carbon nanotubes. Low- (a) and high-magnification (b) SEM images of pin-like nanotubes. (c–e) SEM images of three typical tube tip morphologies. The insets are the corresponding TEM images of these three typical tip morphologies. HRTEM images taken at one side of a hollow tube body (f) and the joints of the tip and tube (g).

show that the nanotubes have a pin-like morphology composed of an oval-shaped tip filled with liquid Ga and a tapered hollow body [Fig. 4(b)]. The diameters of the tapered tubes vary from ~50 nm at the thinner parts to ~200 nm at the thicker parts, and the length of the tubes is in the range of 4 to 8 μm. The oval-shaped tips have a maximum diameter in the range of 200–500 nm and length of up to 2 μm. The wall of the nanotube is so thin that the hollow structure of the tube, the tube walls, and the Ga level inside can be clearly seen even with the SEM operated at 5 kV. Three kinds of tip morphologies can be distinguished: the first has a flat tip front [Fig. 4(c)]; the second has a Ga-filled sharp end [Fig. 4(d)]; and the third has a short open tube that extrudes from an oval-shaped ball [Fig. 4(e)]. Figure 4(f) shows a HRTEM image of one side of a hollow tube, and Fig. 4(g) shows the joint part of the tip and tube body (the black part is Ga). It is clear that the tubes are multi-walled carbon nanotubes. Both SEM and TEM results indicate that the nanotubes present here have a very large inner-outer diameter ratio with a value of >0.9, which is much larger than that of conventional nanotubes (usually <0.5).

We heated the Ga-filled carbon nanotubes in situ in TEM in the temperature range of 30–850°C and found that below 550°C, the Ga inside the tube tip expanded almost linearly along the hollow tube with the temperature, with an average increase of ~20 nm/100°C. This means that the Ga-filled nanotubes might work as a nanothermometer in the temperature range of 30–550°C, which might be suitable for use in a wide variety of microenvironments.

(d) Gallium-catalyzed growth of SiO_x nanowire assemblies[7,8]

Figure 5 shows the SEM and TEM images of Ga-catalyzed SiO_x nanowire assemblies by using SiH_4 as the Si source. Electron microscopy observations reveal that the morphologies of the products are very sensitive to the growth temperature. From the highest deposition temperature of 1100°C to the lowest deposition temperature of 950°C (covering a substrate length of ~45 mm), the morphology, distribution, and density of the products vary gradually with their positions on the alumina substrate and five distinctive deposition zones can be identified based on the morphologies of the products. From 1100°C to 950°C, the morphologies of the products change from fishbonelike (Zone I, 1100–1050°C) [Fig. 5(a)] to gourdlike (Zone II, 1050–1030°C) [Fig. 5(c)], spindlelike (Zone III, 1030–1010°C) [Fig. 5(d)], badmintonlike (Zone IV, 1010–980°C) [Fig. 5(e)], and finally octopuslike (Zone V, 950–980°C) [Fig. 5(f)]. However, although the products formed in different temperature zones have different morphologies, they share some similar structural and compositional features. For example, as shown in Fig. 5, all the products are composed of a spherical liquid Ga

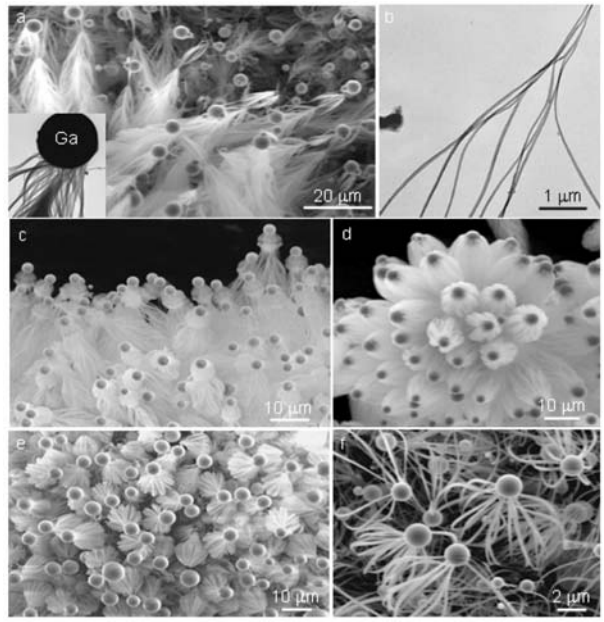

Fig. 5. SEM and TEM images of Ga-catalyzed SiO_x nanowire assemblies by using SiH_4 as the Si source. (a) Fishbonelike SiO_x nanowire assemblies formed in Zone I (1050–1100°C), showing typical batch-growth feature. The inset shows a TEM image of the tip part of a fishbonelike structure, showing many SiO_x nanowires growing out from the lower hemisphere surface of a Ga ball. (b) TEM image of a nanowire bundle displaying branching-growth phenomena. (c) Gourdlike SiO_x nanowire assemblies formed in Zone II (1030–1050°C). (d) Spindlelike SiO_x nanowire assemblies formed in Zone III (1010–1030°C). (e) Badmintonlike SiO_x nanowire assemblies formed in Zone IV (980–1010°C). (f) Octopuslike SiO_x nanowire assemblies formed in Zone V (950–980°C).

ball and a silicon oxide nanowire bunch that is composed of numerous highly aligned amorphous silicon oxide nanowires with diameters of 40–80 nm and lengths of 10–20 μm. These complex morphologies can be well explained by two novel nanowire growth phenomena that were mainly observed in silicon oxide nanowire growth. One growth phenomenon is the branching growth, that is, one nanowire splits into two branches, and the newly formed branch also splits into two subbranches, and so on [Fig. 5(b)]. The other phenomenon is the batch growth; that is, the nanowires within a bunch tend to grow batch by batch so that the nanowire bunch can be regarded as a rick piled up with nanowires [see Fig. 5(a) as an example and refer to ref. 7 for detailed growth mechanism].

Figure 6 shows the SEM images of Ga-catalyzed SiO_x nanowire assemblies by using SiO powder as the Si source. The morphologies of the products formed by using SiO powder as the Si source are different from those formed from SiH_4. Figure 6(a) is a SEM image showing highly aligned and closely packed rodlike structures. Most of the rods have a carrotlike morphology with a sandwichlike topology that consists of three materials with different morphologies, states, and crystallographic structures [Figs. 6(b) and 6(c)]. The "carrot" top is a liquid Ga ball

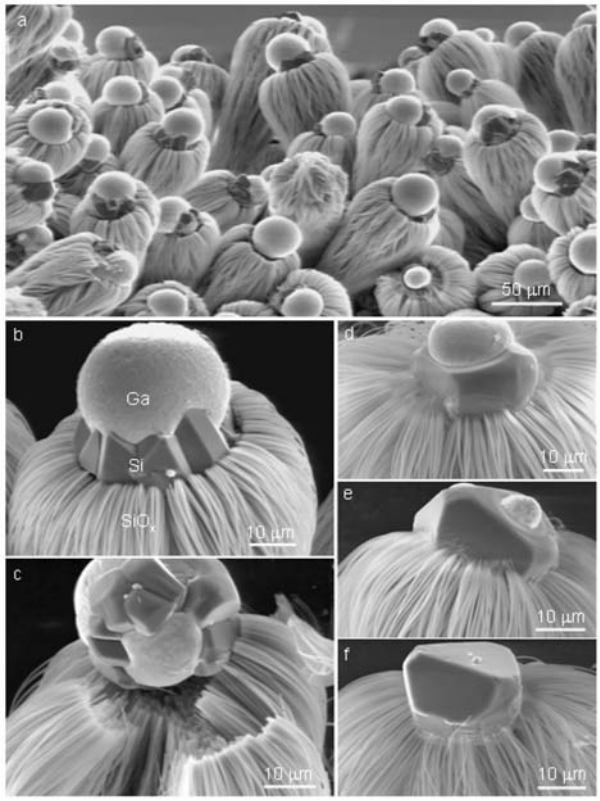

Fig. 6. SEM images of Ga-catalyzed SiO_x nanowire assemblies by using SiO powder as the Si source. (a) Low-magnification SEM image of the as-grown products, showing highly aligned and closely packed rodlike structures. Close-up view of the top part of an as-grown (b) and opened (c) sandwich-structured rod, revealing that the rod is composed of three materials with different morphologies, states, and crystallographic structures, as well as the relationship among these three parts. (d) A sandwichlike rod having a hemispherical Ga droplet on the top surface of a Si polyhedron. (e) A sandwichlike rod having two small hemispherical Ga droplets on the two top surfaces of a Si polyhedron. (f) A rod consisting of a polyhedral Si tip and a nanowire bunch.

with diameter of ~10 to 30 µm; the shoulder (middle part) is a Si ring usually composed of ~10 micrometer-sized, clearly faceted and crystalline Si polyhedrons that are arranged sequentially around the lower hemisphere surface of the Ga ball; the bottom part is a carrot-shaped bunch (~60 µm in maximum diameter and up to 200 µm in length) of highly aligned silicon oxide (SiO_x, $x = 1.5–2$) nanowires that grow perpendicularly from the downward facing facets of the Si polyhedrons. Besides the rods shown in Fig. 6(b), we also observed two other kinds of morphologies as shown in Figs. 6(d–f). Figure 6(d) and 6(e) show two typical derivatives of sandwichlike rods, respectively displaying 1 to 2 small hemispherical Ga droplets (5–15 µm in diameter) located on the top facets of a large Si polyhedron (~20 µm in width and 10–20 µm in height). In Fig. 6(f), however, the rod consists only of a polyhedral Si tip and a carrot-shaped nanowire bunch; no Ga droplet was observed on the Si crystal surface. Note that the batch-growth and branching-growth phenomena were also observed in the silicon oxide nanowire assemblies prepared from SiO powder.

Summary and Conclusions

As demonstrated in this project, well-aligned carbon nanotubes and quasi-aligned single-crystalline Ge nanowires were grown on mesoporous silica thin films doped with Fe and Au nanoparticles, respectively. Specially, the sol-gel-prepared silica film can be easily cast into patterned substrates by simply using TEM grids as the shadow masks so that aligned carbon nanotube patterned can be obtained. Because no sophisticated facilities such as lithography were involved in preparing the catalyst patterns, our technique represents a simple, low-cost approach to the micropatterning of aligned carbon nanotubes. These low-cost nanotube micropatterns might find application in the area of flat panel displays.

In this project, molten Ga was proved to be an effective catalyst for high-yield growth of carbon nanotubes and complex SiO_x nanowire assemblies. The Ga-catalyzed growth demonstrated several interesting new growth phenomena unlike any previously observed by using high-melting point Au and Fe as the catalysts, which greatly enrich the current VLS growth mechanism.

References

[1]J. Hu, W. Odom, and C. M. Lieber, "Chemistry and Physics in One Dimension: Synthesis and Properties of Nanowires and Nanotubes," *Acc. Chem. Res.* **32**, 435–445 (1999).

[2]R. S. Wagner and W. C. Ellis, "Vapor-Liquid-Solid Mechanism of Single Crystal Growth," *Appl. Phys. Lett*. **4**, 89–90 (1964).

[3]Z. W. Pan, H. G. Zhu, Z. T. Zhang, H. J. Im, S. Dai, D. B. Beach, and D. H. Lowndes, "Patterned Growth of Vertically Aligned Carbon Nanotubes on Pre-patterned Iron/Silica Substrates Prepared by Sol-Gel and Shadow Masking," *J. Phys. Chem. B* **107**, 1338–1344 (2003).

[4]Z. W. Pan, H. G. Zhu, Z. T. Zhang, H. J. Im, S. Dai, D. B. Beach, and D. H. Lowndes, "Hierarchically Ordered Carbon Tubes," *Chem. Phys. Lett.* **371**, 433–437 (2003).

[5]Z. W. Pan, S. Dai, and D. H. Lowndes, "Straight Single-Crystalline Germanium Nanowires and Their Patterns Grown on Sol-Gel-Prepared Gold/Silica Substrate," to be submitted.

[6]Z. W. Pan, S. Dai, D. B. Beach, N. D. Evans, and D. H. Lowndes, "Gallium-Mediated Growth of Multiwall Carbon Nanotubes," *Appl. Phys. Lett.* **82**, 1947–1949 (2003).

[7]Z. W. Pan, S. Dai, D. B. Beach, and D. H. Lowndes, "Temperature Dependence of Morphologies of Aligned Silicon Oxide Nanowire Assemblies Catalyzed by Molten Gallium," *Nano. Lett.* **3**, 1279–1284 (2003).

[8]Z. W. Pan, S. Dai, D. B. Beach, and D. H. Lowndes, "Liquid Gallium Ball/Crystalline Silicon Polyhedrons/Aligned Silicon Oxide Nanowires Sandwich Structure: An Interesting Nanowire Growth Route," *Appl. Phys. Lett.* **83**, 3159–3161 (2003).

Multifunctional Nanotube Composites

D. B. Geohegan,[1] P. F. Britt,[2] M. J. Lance,[3] A. A. Puretzky,[4] M. A. Guillorn,[5] M. Dadmun,[6] J. Devenyi,[7] A. Pedraza,[4] I. Ivanov,[1] H. Schittenhelm,[2] S. Viswanathan,[2] A. Rasheed,[4] S. N. Jesse,[6] B. White,[8] J. Y. Howe,[3] and K. Belay[9]

[1]*Condensed Matter Sciences Division*
[2]*Chemical Sciences Division*
[3]*Metals and Ceramics Division*
[4]*Materials Science and Engineering Department, University of Tennessee*
[5]*Engineering Science and Technology Division*
[6]*Department of Chemistry, University of Tennessee at Knoxville*
[7]*Department of Chemistry, University of Tennessee at Martin*
[8]*ERULF summer student, Saginaw Valley State University*
[9]*Visiting HBCU Faculty Program Participant, Florida A&M University*

This project focused on the development of new composite materials incorporating carbon nanotubes. The light weight, great strength, and high electrical and thermal conductivities of single-walled carbon nanotubes (SWNTs) are envisioned to lend new functionality to matrices of polymers, carbon, and metals. This project developed new capabilities in the synthesis and processing, characterization, and testing of multifunctional nanocomposites using nanotubes. First, coordinated laser-vaporization synthesis and chemical purification procedures were developed to produce the purest (>99.98 wt %) SWNTs known, an essential starting point to understand nanotube chemistry for strong bonding in polymer composites. Second, several novel processing techniques were developed to align the nanotubes and infiltrate them with matrix materials in order to form composites with directional electrical and thermal conductivity. Controlled aggregation techniques were developed to form pure SWNT papers and fibers. Electrospinning was developed to make polymer fibers containing aligned SWNTs. Pulsed laser deposition was used to coat and protect SWNT networks with amorphous diamond films. Infiltration techniques were used to encapsulate millimeters-long, vertically oriented arrays of carbon nanotubes (multiwall plus single wall). Finally, methods of imaging and testing the properties of these materials were developed, including (1) a new electron microscopy technique capable of imaging nanotubes within thin polymer films, (2) polarized Raman microscopy to measure nanotube alignment, and (3) Raman spectroscopy analysis of strain within thin composite films. The carbon nanotube chemistry, physics, and processing methods developed in this project resulted in nanoscience techniques, which greatly enhanced capabilities at ORNL, and prototype nanotube–based composites that have attracted interest from several federal agencies.

Introduction

Single-wall carbon nanotubes are exceedingly strong (>1 TPa axial Young's modulus) and have been theoretically predicted to form strong, lightweight composites far superior to those used today in aerospace, transportation, and commercial products. In addition to strength, their remarkable electronic and thermal properties have been envisioned to lend additional functionality to polymers, especially if the nanotubes can be aligned within the polymer matrix. However, due to a poor understanding of nanotube chemistry, good dispersion of nanotube bundles and strong bonding to polymer matrices have not been generally achieved and the predicted strength enhancements have not been realized. Moreover, reliable methods have not been developed to induce and measure nanotube alignment or methods to image and characterize electronic transport through nanotube networks in polymers. This project addressed these scientific needs and, through the fabrication of prototype nanotube-polymer composites, experimentally explored the improvements in polymer properties induced by carbon nanotubes.

Technical Approach

A major goal of this project was to understand how the synthesis conditions of single-wall carbon nanotubes (SWNTs) affect their chemistry during their purification. Irreproducible nanotube chemistry is largely attributable to chemical treatments employed to remove unwanted metal catalyst nanoparticles formed during their synthesis

and the resulting residual unconverted carbonaceous impurities which adhere to the walls of the nanotubes after these treatments. Laser vaporization was used to synthesize SWNTs at ORNL.

The technical approach for the chemical purification and functionalization of the nanotubes is outlined in Fig. 1. Raman spectroscopy of characteristic SWNT optical modes was used to gauge the yield of nanotubes in the raw material as well as the level of defects they contained, and all material was examined by scanning electron microscopy through each step of the purification procedure. Since SWNTs oxidize at higher temperatures than amorphous carbon (a-C), thermogravimetric analysis (TGA) was used to infer the fraction of SWNTs vs a-C after removal of the metal catalyst. Inadvertent variations in the synthesis conditions were found to affect the level of graphitic carbon–coated metal nanoparticles observed by TEM, so synthesis conditions were adjusted to minimize these while preserving high nanotube yields. The approach in this project of jointly synthesizing and purifying SWNTs differs from the general practice of purchasing SWNTs from vendors and attempting to perform reproducible chemistry; however, the successful reproducible achievement of ultrapure SWNTs (>99.98 wt %, as measured by ICP analysis) is a major accomplishment of this program which has not been achieved elsewhere.

Various approaches were derived to solubilize the nanotubes in various solvents and mix them with solubilized polymers to form stable nanotube-polymer solutions. To enhance the solubility of the SWNT in solvents, improve polymer-SWNT interactions, and enhance the dispersion of SWNT bundles, methods were explored to functionalize the SWNTs. Typically, the carboxyl groups (-COOH) produced from the oxidative purification of crude SWNTs are derivatized with long-chain alkyl groups to improve solubility. Unfortunately, FTIR analysis revealed that the purified SWNTs had no detectable carboxyl groups. Thus, various methods, including KNO_4, acids, and ozone, were attempted to introduce carboxyl groups into the pure SWNT without producing amorphous carbon.

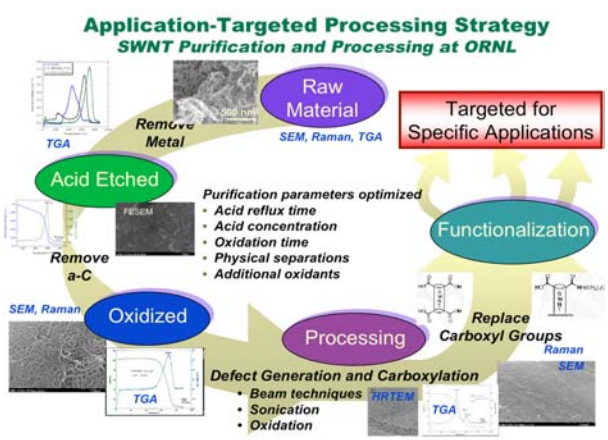

Fig.1. Chemical methods developed to purify ultrapure (>99.98 wt %) single-wall carbon nanotubes from "raw" 50 wt % material produced by laser vaporization, then functionalize them for use in polymer composites. Coordinated SEM, Raman, TGA, and HRTEM techniques are used to gauge effectiveness of acid-etching and selective oxidation steps to remove metal catalyst and amorphous carbon impurities. Synthesis conditions are readjusted to improve these steps. Once high-purity SWNTs are obtained, defects are reintroduced and assessed, enabling reproducible functionalization chemistry to be performed.

Nanotube-polymer composites were then formed from these solutions by spinning them onto silicon wafers with prepatterned electrodes, doctor-blading them into thin sheets, or electrospuning them into fibers. Alternatively, purified nanotubes in solvents were formed into aligned, pure nanotube papers and fibers through controllable aggregation using electric fields, drying techniques, shear flow, or combinations of these. Special consideration was given to methods of composite processing that simulataneously produced alignment of SWNTs in the finished composite. In addition, polystyrene composites containing 1 and 2 wt % octadecyl functionalized SWNTs were prepared by precipitation of a well-mixed solution of polystyrene and functionalized SWNTs followed by melt pressing the material into a bar.

To assess alignment of nanotubes within fibers, blocks, and thin films, several approaches were developed. Polarized resonant Raman scattering utilized the high anisotropy of the Raman scattering signal from SWNTs *along* vs *perpendicular* the nanotube length. In addition, frequency shifts of the characteristic nanotube breathing and tangential modes with strain were explored to understand load transfer of applied stress to nanotubes embedded in the composite.

Novel approaches were developed to characterize the composites and assess their mechanical, electrical, and thermal properties. Electrical conductivity of nanotube-polymer (PMMA) composites was explored in a specially fabricated scanning electron microscopy (SEM) stage which permitted the current-voltage characteristics of embedded nanotube networks to be recorded *while simultaneously imaging their morphology inside the polymer.*

Results and Accomplishments

Some of the highest-purity SWNTs produced worldwide were accomplished in this project, and are shown in Fig. 2. A wide variety of chemical oxidative treatments, including nitric acid, nitric/sulfuric acid, hydrogen peroxide, hydrogen peroxide/sulfuric acid, $KMnO_4$/sulfuric acid, as well as steam and thermal

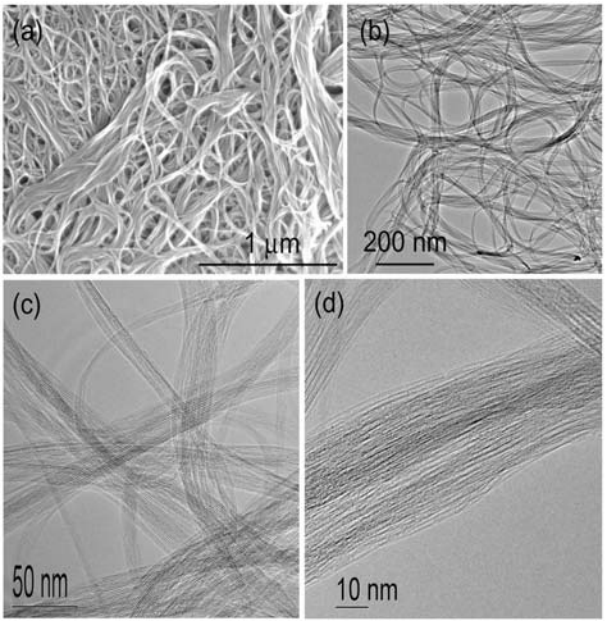

Fig. 2. Single-wall carbon nanotubes grown by laser vaporization and purified according to the procedure of Fig. 1 to remove metal catalyst nanoparticles (to <0.02 wt %) and amorphous carbon impurities. (a) Large-area scanning electron microscope image, (b) TEM image, and (c,d) HRTEM images of nanotube bundles. These SWNT are among the purest reported and serve as an important benchmark for purity and a starting point for reproducible nanotube chemistry.

oxidative treatments, were evaluated to remove the metal and carbon impurities while maintaining a reasonable yield of purified SWNTs. The carbon coating on the metal catalyst particles was notoriously difficult to remove without destroying the SWNTs. Moreover, the oxidative stability of the carbon impurities were found to be very sensitive to the laser ablation conditions so that each batch of crude SWNT had to be screened by TGA, FESEM with EDX, TEM, and Raman spectroscopy and the purification procedure optimized. Overall, the best purification method involved refluxing crude SWNT in 3 *M* nitric acid for 16 h, filtering, and optimizing the thermal oxidation treatment by TGA and FESEM (with EDX) assessment. Acid-refluxed samples were typically heated to 400 °C for 2 h in air, sonicated in concentrated HCl for 10 min, and washed with water. The samples were then subjected to a second thermal oxidation at 450 °C for 3 h, sonicated in concentrated HCl/HF, and washed with water. The two-stage thermal oxidation was necessary to enhance the yield of pure SWNTs. The final product was obtained in 8.0 ± 1.3% yield and contained <0.025 wt% Ni and Co (by ICP) and a very low content of amorphous carbon, by TEM and NIR measurements. These samples appear to be some of the highest purity SWNTs produced anywhere to date.[1]

A wide variety of novel processing techniques were developed to form nanotube-polymer and nanotube-carbon composites targeting several key application areas. Thin films, fibers, and blocks were obtained with greatly enhanced electrical and thermal conductivity. Several are shown in Fig. 3. The first SWNT-amorphous diamond composite films were formed by pulsed laser deposition of pure C onto dried, spray-deposited SWNT solutions while the electrical properties of the nanotube networks were monitored in situ. The conduciting nanotube networks were coated and protected with transparent, amorphous diamond [Fig. 3(a,b)] to form a novel all-carbon composite which were highly scratch resistant and of interest for applications as sensors and smart coatings.[2]

Thin films of nanotube-polymer composites were also formed [Fig. 3 (c, d) and Fig. 4]. Due to the poor contrast difference between carbon nanotubes and polymers in TEM, the morphology of embedded nanotube networks are virtually impossible to reveal nondestructively. In this project, it was discovered that nanotubes could be imaged *inside the polymer thin film* by scanning electron microscopy using certain bias conditions of the sample and accelerating voltages of the electron beam (Fig. 4).[3] These measurements provided *the first coordinated measurements of nanotube network morphology and conduction* inside polymers to understand how junctions

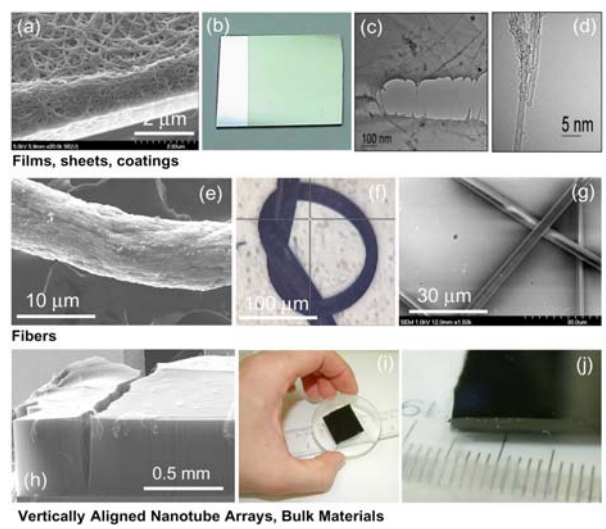

Fig. 3. Processing techniques were developed to form nanotubes into functional composites. (a, b) SWNT dried from solution after spray-deposition onto Si were coated with amorphous diamond by pulsed laser deposition to form highly scratch-resistant, transparent, electrically conductive coatings. (c,d) SWNTs encapsulated inside polymers (e.g., PMMA) by spin-deposition of nanotube-polymer solutions were investigated by HRTEM. (e) Neat fibers of SWNT formed by shear forces, solvent replacement, and flocculation of "nanotube ink." (f, g) Electrospun nanotube-polymer fibers (PMMA and PEO, respectively). (h) As-grown, vertically aligned array of multiwall carbon nanotubes. (i, j) Epoxy-infiltrated vertical MWNT arrays with preserved nanotube alignment.

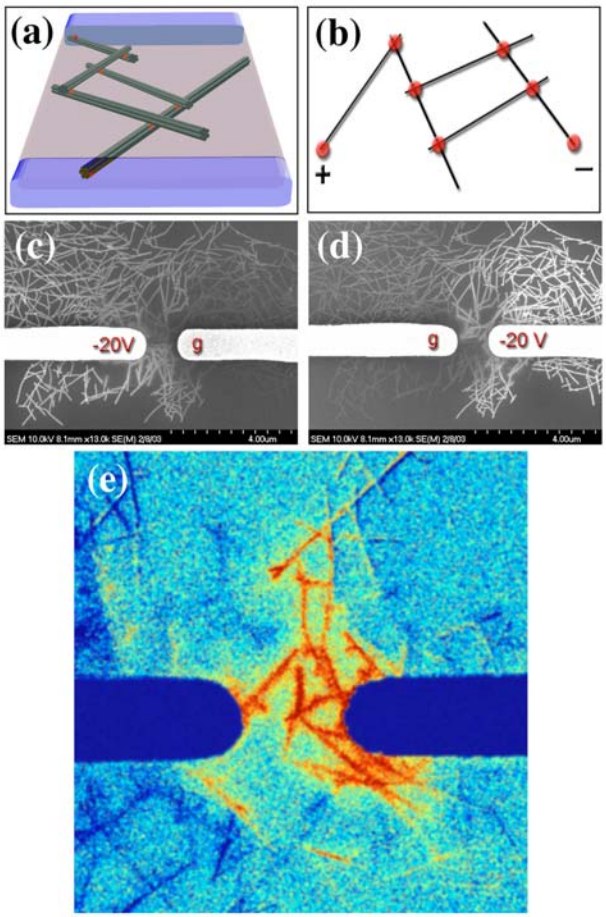

Fig. 4. Nanotubes lend orders-of-magnitude increase in electrical conductivity to polymers; however, nanotubes occur mainly in bundles as shown in (a), which shows a series of nanotube bundles inside a thin polymer film spanning two electrodes (blue). Connections between the nanotube bundles lead to an equivalent circuit as shown in (b). In this project, an electron microscopy technique was developed to image SWNT bundle networks inside *polymer films while they carried current between biased electrodes. As shown in (c) and (d), nanotube bundles (white) between grounded (g) or negatively biased (-20V) electrodes in PMMA are directly visible due to enhanced contrast induced by the electric field effect on secondary electron emission. The nanotubes participating in the measured current-voltage characteristic can be determined by image processing, as shown in (e).*

between nanotube bundles lead to overall conductivity of the composite. In addition, the conditions responsible for enhanced contrast between the nanotubes and the polymer were studied and analyzed and found to relate to the shift in secondary electron yield caused by electric fields in the test fixture. This technique appears to be a new, general one in electron microscopy we call *electric field–induced contrast* imaging. The electrical conductivity of SWNT networks in thin poly-methyl methacrylate (PMMA) films was measured vs weight loading, and over four-orders-of- magnitude increase was obtained with less than 1 wt % nanotubes.

For nanotube-polymer composites with directional electrical and thermal conductivity, nanotubes must be aligned. Fibers composed of aligned nanotubes are natural forms which satisfy this requirement. Graphitic carbon fibers are a mainstay of composite manufacturing, and SWNT fibers are predicted to have much higher strength and electrical/thermal conductivity. Neat nanotube fibers and aligned nanotube papers were formed by solubilizing SWNT in surfactants such as sodium dodecyl sullfate, then inducing aggregation during shear extrusion into another liquid or during drying on a plate at the meniscus. Long, hairlike prototype SWNT fibers were tested for mechanical strength and found to be remarkably strong (supporting over 30 g of weight for a 10-mm-diameter fiber). Electrospinning was developed in this project to synthesize nanotube-polymer fibers of over 15 polymers with diameters ranging from 100 µm down to 100 nm. Electrospinning involves high voltage to draw fibers from droplets of viscous (nanotube-polymer) solution. The nanotube alignment within the pulled fibers was determined by polarized Raman microscopy, with SWNT becoming highly aligned (18:1 polarization ratio) for fiber diameters less than 10 mm. In general, significant enhancements in the oxidative thermal stability (75°C for PMMA) were observed at low weight loadings (0.6 wt %) of SWNT—an important enhancement allowing polymers to be used in applications at elevated temperatures.

To enhance the solubility of the SWNT in solvents, improve polymer-SWNT interactions, and to enhance the dispersion of SWNT bundles, methods were explored to functionalize the SWNTs. Typically, the carboxyl groups (-COOH) produced from the oxidative purification of crude SWNTs are derivatized with long-chain alkyl groups to improve solubility. Unfortunately, FTIR analysis revealed that our pure SWNTs had no detectable carboxyl groups. Thus, various methods, including KNO_4, acids, and ozone, were attempted to introduce carboxyl groups into the pure SWNT without producing amorphous carbon. The best method involved treating SWNTs with piranha solution (a 4:1 mixture of 30% hydrogen peroxide and sulfuric acid) for 1 h at 70 °C. The carboxylated nanotubes were reacted with thionyl chloride ($SOCl_2$) followed by octadecylamine ($C_{18}H_{37}NH_2$) to produce octadecyl functionalized SWNT. This material could be suspended in organic solvents, such as ethylene dichloride, for >1 week while the unfunctionalized SWNTs would precipitate in a few hours. Attempts to produce a water-soluble SWNTs by functionalization with poly(ethylene glycol) monomethyl ether were unsuccessful.

Polystyrene composites containing 1 and 2 wt% octadecyl functionalized SWNTs were prepared by precipitation of a well-mixed solution of polystyrene and functionalized SWNTs followed by melt pressing the

material into a bar. The black composites containing functionalized and pure SWNTs were analyzed by dynamic mechanical analysis. Overall, the glass transition temperature, determined from the maximum of tan *d*, was not significantly affected (±5 °C) by the addition of the SWNTs to the polymer. However, the storage modulus (E') at room temperature increased 57% for polystyrene plus 1wt % functionalized SWNTs, and a factor of 4.8 for polystyrene plus 2 wt % functionalized SWNTs compared to polystyrene alone. The storage modulus was also 60% larger for the functionalized SWNT than for the pure SWNTs. To investigate the dispersion of the functionalized SWNTs in the polystyrene, thin films were cast and examined by SEM analysis. Although large bundles of SWNTs were observed in the composite, the functionalized nanotubes appeared to be better dispersed than the non-functionalized SWNTs. Although functionalization did not significantly enhance the dispersion the bundles of SWNT, the mechanical properties of polystyrene were enhanced with low loading of SWNTs indicating load transfer between matrix and filler.

Finally, aligned multiwall carbon nanotubes grown by chemical vapor deposition into long arrays [Fig. 3 (h)] were infiltrated by epoxies to form composites which were electrically and thermally conductive [Fig. 3(i,j)]. Alignment of the nanotubes was preserved during polymer infiltration, resulting in an increase in thermal diffusivity of a factor of 20 compared to the epoxy alone, as measured by flash photolysis. Nanoindentation measurements of the composites both along and perpendicular to the nanotube axes revealed no change in hardness; however, a 47% increase in Young's modulus parallel to the nanotube axis was noted.

Summary and Conclusions

The chemistry of SWNTs and their processing into functional nanotube-polymer and nanotube-carbon composites were explored in this project. The *highest-purity SWNTs* reported were obtained in this project, distinguishing ORNL as a leader in combined SWNT synthesis and chemistry. Chemical functionalization of the nanotubes was studied and used to enhance the solubility and dispersion of the nanotubes in polymers, resulting in significantly higher strength (storage modulus, up to a factor of 5 higher for polystyrene). Electrical properties of nanotubes in polymers were studied through the development of an electric field–induced contrast-imaging electron microscopy technique, which permitted SWNT bundles and networks to be imaged during current flow in polymers for the first time. Several processing and characterization techniques were developed at ORNL to incorporate nanotubes into polymers, including electrospinning, shear, electrophoresis, fiber extrusion, and infiltration of vertically aligned nanotube arrays.

This project resulted in a wealth of new science involving the chemistry of carbon nanotubes which will enhance other DOE programs in both basic science (DOE-DMS/BES work at the Center for Nanophase Materials Sciences at ORNL and the other DOE nanoscience centers) and applied research (e.g., DOE-EERE Hydrogen and Fuel Cells programs). The protoype multifunctional nanotube composites developed in this project were prototypes designed not only for lightweight, fuel-efficient transportation vehicles with enhanced strength for DOE but for other government agencies (especially NASA, DARPA, and other DoD agencies).

Formal presentations have been made to secure follow-on funding at DARPA, NASA-Langley, NASA-Marshall, AMCOM, and TARDEC, with approximately five white papers prepared to date. DARPA is interested in thin multifunctional nanotube-polymer skins with optoelectronic, sensing, and energy storage capabilities. DARPA, NASA, and AFRL are all interested in the thermal management offered by embedded heat pipes formed by nanotubes in space age polymers. The Army is interested in nanotube-based materials for lighter-weight tanks and vehicles, as well as the optical limiting properties nanotubes offer embedded in transparent polymers. Most government agencies (especially NASA) have well-defined timelines for progress in nanotube-based composites. Our project—through the basic science and the resulting protoype composites it enabled—directly meshed with their needs, advancing their timelines and providing the scientific basis for continued efforts in this area.

References

[1]P. F. Britt. S. Viswanathan, D. B. Geohegan, I. Ivanov, A. A. Puretzky, J. Howe, H. Schittenhelm, B. White, "Preparation of High Purity Single-Wall Carbon Nanotubes Synthesized by Pulsed Laser Vaporization" (submitted).

[2]H. Schittenhelm, D. B. Geohegan, G. E. Jellison, A. A. Puretzky, M. J. Lance, P. F. Britt, "Synthesis and Characterization of Single-Wall Carbon Nanotube–Amorphous Diamond Thin-Film Composites," *Appl. Phys. Lett.* **81**, 2097 (2002).

[3]S. Jesse, M. A. Guillorn, I. N. Ivanov, A. A. Puretkzy, J. Y. Howe , P. F. Britt, and D. B. Geohegan, "Electron Microscopy Imaging of Single-Wall Carbon Nanotube Networks in Polymers" (submitted to *Nanoletters*).

Multiscale Modeling and Simulation of the Growth and Functionalization of Nanotube Crystals, Arrays, and Polymeric Composites

R. F. Wood,[1] D. W. Noid,[2] S. Pannala,[2] B. G. Sumpter,[2] J. C. Wells,[2] and Z. Zhang[1]
[1]*Condensed Matter Sciences Division*
[2]*Computer Sciences and Mathematics Division*

Calculations on both continuum and atomistic models were carried out as part of multiscale simulations of carbon nanotube nucleation and growth. The continuum model is used to demonstrate the key roles played by the size and shape of the catalytic particle in conjunction with the concentration and temperature gradients at the gas/solid interface and in the catalytic particle. First-principles electronic structure calculations relating to the formation of single-wall carbon nanotubes were carried out. Density-functional theory in various forms was used throughout. A 38-atom Ni cluster and several low-index Ni surfaces were investigated using pseudopotentials and plane-wave expansions. The energetic ordering of the sites for carbon atom adsorption was found to be the same, with the Ni(100) facet favored. In other calculations, Gaussian orbital basis sets were used to study a cluster or "flake" containing fourteen carbon atoms. The flake is a segment of three hexagons from an "unrolled" carbon nanotube, with an armchair termination. The binding energies of C, Ni, Co, Fe, Cu, and Au atoms to it were calculated to gain insight into the mechanism for the high catalytic activity of Ni, Co, and Fe and the lack of it in Cu and Au.

Introduction

The importance of nanoscience to advanced materials development and the potential opportunities associated with it have been repeatedly emphasized during the last decade. Within the nanoscience area, carbon nanotube (CNT) research is arguably the most likely to yield dramatic near-term results if certain issues can be resolved. Nanotubes are lightweight, exceptionally strong, and have excellent thermal properties. Their incorporation into composite materials could revolutionize a wide range of advanced structural materials. Likewise their electronic properties, particularly of single-wall carbon nanotubes (SWNT), have proved to be fascinating, exhibiting electrical conductivity that varies from metallic to semiconducting to insulating, depending on the growth conditions. It has also been claimed that carbon nanotubes can be a storage medium for atomic hydrogen. Unfortunately, there are daunting roadblocks to the development and commercialization of CNT technologies. As yet, there are no methods for growing nanotubes in the quantities and with the purity needed. And once grown, the separation of various types (single wall, multiwall, aligned, etc.) is time-consuming, unreliable, and costly. Also, there is no way at this time to control the electrical properties by growing nanotubes with specified diameter, length, and chirality.

Paramount among the issues impeding the development of CNT materials is the role of the metal catalyst, which is still completely unclear even for the simplest growth technique. It is widely agreed that a much better understanding of the nucleation and growth processes is needed. Since in situ techniques for directly observing the growth are not likely to be available anytime soon, simulation of the processes at some level is almost mandatory. But the time and space scales involved cover many orders of magnitude, and the mathematical and computational aspects of such "multiscale" problems are formidable. For example, first-principles, quantum-mechanical molecular dynamics (MD) calculations extensive enough for reliable parametric studies, even on a picosecond time scale, are well beyond the capabilities of current computers. Conversely, classical interaction potentials for dissimilar atoms embedded in a complex atomic environment, which might greatly speed up the MD calculations, have proved virtually impossible to construct. Consequently, the multiscaling used to date for the type of problems addressed here is at a relatively modest level. It consists mainly of using continuum and atomistic models in a complementary fashion to extract information of most interest to the experimentalists. Our efforts in this direction are described here.

Technical Approach

The approach taken in the research had two main focal points. In the first, CNT growth was studied using a continuum model based on coupled heat and mass

transport partial differential equations. The MATLAB program with the Partial Differential Equation (PDE) toolbox was used extensively. This provided a powerful and flexible framework in which to cast the continuum modeling. Unlike previous research on the growth of carbon nanotubes and nanofibers,[1] it was possible to use a finite element method (FEM) with unstructured grids, adaptive mesh refinement (AMR), etc., that greatly expanded the range of geometries that could be considered. A schematic of the continuum model for CNT growth in the so-called tip-growth mode is shown in Fig. 1.

The geometry in the figure was chosen based on a frequently observed shape of the catalyst. It was found that slight variations in the shape do not change the predictions drastically. An earlier two-dimension (2-D) simulation[2] for carbon nanofibers employed geometry similar to that of Fig.1 but with a simple, highly structured grid. Our grid takes advantage of the 2-D space-filling characteristics of triangles that lead to very efficient numerical integration algorithms. This unstructured, adaptive grid is optimized simply by changing the size and shape of the triangular elements over the computational domain, as needed for convergence. In fact, for steady-state calculations, the AMR feature of the computer program can be used to refine the grid based on a variety of criteria.

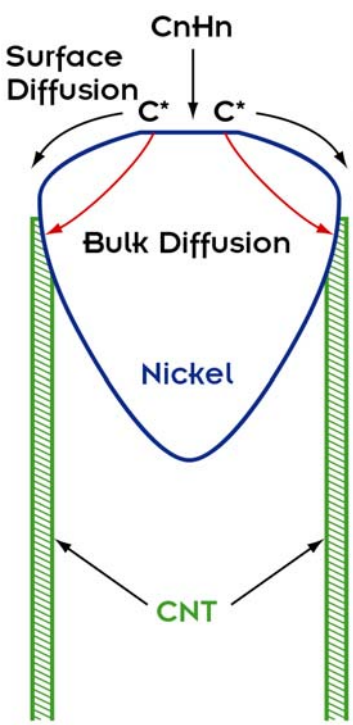

Fig. 1. Carbon nanotuibe growth via the tip growth mode. For a nanotube diameter of 1–2 nm, the catalytic particle is in the mesoscopic regime.

The other focal point included first-principles, atomistic calculations of several types of structures thought to be relevant to CNT formation. All of these calculations utilized density functional theory (DFT) as implemented in a number of readily available computer codes. In one set of calculations, pseudopotentials and plane wave expansions of the wave function were used, while in another, expansion of the wave function was carried out in Gaussian basis sets. In the latter approach, the NW Chem suite of programs developed at Pacific Northwest National Laboratory was employed.

Results and Accomplishments

Mesoscopic Continuum Model

Previous continuum modeling efforts in ref. 1 were directed to the growth of carbon filaments and fibers rather than single and multiwall nanotubes. In carbon filament growth, the carbon diffusion through the rather large catalytic particle is usually the rate-limiting step, and thus those studies cannot be extrapolated simply to the CNT growth from quite small particles. Also, using the latest advances in computational methods mentioned above, one can now simulate more complicated shapes and sizes of catalyst particles very efficiently. Later, the complexity of the calculations can readily be expanded to include interfacial dynamics.

Our starting point for these calculations was a set of coupled equations for heat and mass diffusion.[3] After considerable simplification of the diffusion equation, and with an assumption that steady-state growth has been reached, the mass diffusion equation can be reduced to

$$\frac{\partial}{\partial r}\left(rD(T)\frac{\partial Y_c}{\partial r}\right)+\frac{\partial}{\partial z}\left(rD(T)\frac{\partial Y_c}{\partial z}\right)=0 \ ,$$

where Y_c is the carbon mass fraction, r the radial coordinate, z the axial coordinate, D the diffusion coefficient, and T the temperature. In principle, D is a function of both T and Y_c but since experimental data is not available for its dependence on the C concentration, only the T-dependence was considered. It was assumed to have the classical form $D(T) \sim \exp(-E/kT)$, in which E is an activation energy.

The above equation was solved with appropriate boundary conditions (BC). On the top surface (C_nH_n/Ni interface) in Fig. 1, a Dirichlet BC with a specified inlet carbon mass fraction was assigned. At the location where the nanotube is formed (CNT/Ni interface), another Dirichlet BC was specified, with Y_c corresponding to a carbon activity of unity. The outer radius of the nanotube

corresponds to that of the Ni particle, and an inner radius is determined by requiring the wall thickness to be 0.14 nm. On the rest of the Ni particle boundary, a Neumann BC with zero flux was specified.

The calculations show that as time proceeds carbon diffuses into the catalyst particle and the nanotube precipitates out when enough is supplied to the interface where the tube is forming. The concentration in the rest of the particle almost reaches that at the top surface. Thus, the entire particle acts like a reservoir for carbon, part of which diffuses to and is incorporated into the nanotube, while the deficit amount is replenished at the inlet source. This scenario, obtained from the steady-state solution, is also realized by running the transient simulation for extended times.

In the current simulations, three parameters were varied: inlet mass fraction, temperature of the catalyst particle, and the diameter of the Ni particle. The growth rate of the CNT was found, not unexpectedly, to have a linear dependence on the inlet C mass fraction, as shown in Fig. 2(a). This suggests that one way to increase the growth rates is to have surface conditions suitable to maintain higher concentrations.

The dependence of growth rate on particle diameter, Φ, is such that it decreases as the particle size increases. At steady state it is evident that the inlet carbon concentration drives the gradients that exist in the catalytic particle and thus controls the growth rate. The amount of carbon diffused through the top of the catalyst depends on the surface area. From this surface, the carbon diffuses to fill the entire volume of the particle. The surface area varies as the square of the particle diameter, whereas the volume varies as the cube. Consequently, the carbon concentration in the catalyst particle is inversely proportional to Φ. In addition, for the same carbon concentration at the inlet surface, the gradient varies inversely as Φ. This explains the inverse quadratic dependence of growth rate on particle diameter and also the fast growth rates of small diameter SWNTs observed in some experiments.

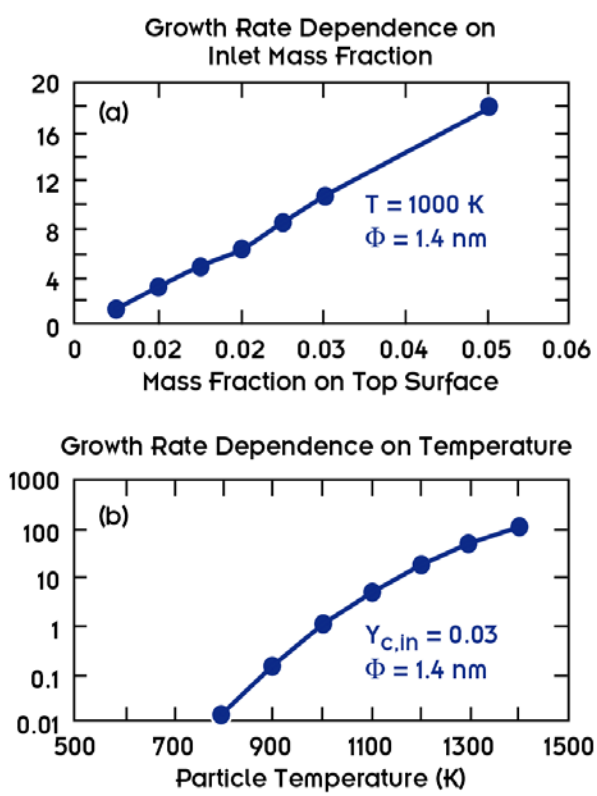

Fig. 2. Growth rate dependence on (a) inlet carbon mass fraction for T = 1000K and CNT diameter Φ = 1.4 nm; and (b) catalyst temperature for inlet carbon mass fraction of 0.03.

Because of the exponential dependence of $D(T)$ on the inverse temperature, the carbon diffusion in the Ni particle has an exponential dependence on temperature and thus the growth rate, which is directly proportional to diffusion, has the expected exponential behavior as shown in Fig. 2(b). The growth rates in these numerical simulations are at least an order of magnitude different from those reported in some experiments where the rate was measured indirectly. In very recent experiments, Geohegan et al.[4] at ORNL have measured growth rates directly by optical interference techniques. Their rates are in much better agreement with the ones shown here.

Perhaps the single most important result of the continuum calculation was one that demonstrated clearly how the number of walls in the CNT is related to the size of the catalytic particle and the concentration of carbon at the top surface. This is important because there is a concerted effort to grow CNTs with only predetermined radii, and it has been unclear how to do it experimentally. We are working closely with the experimentalists in the Condensed Matter Sciences Division on this problem.

Electronic Structure Calculations

An important common feature in the synthesis of single-walled carbon nanotubes is that small clusters of certain transition metals (TM) such as Fe, Co, and Ni are found to be essential to high-yield SWNT formation. The morphologies of SWNTs are directly related to the catalyst particle size. To understand the fundamentals of CNT growth, it is worthwhile to determine which facet is the preferred adsorption site for a carbon atom on TM clusters. Here adsorption energies for carbon nucleation on Ni surfaces were computed by first-principles DFT methods.[5] More specifically, the adsorption of one carbon atom on a 38-atom nickel cluster and on several low-index nickel surfaces was studied.

The results showed that the (100) site is favored for carbon adsorption. The energetic ordering of the sites for carbpm atom adsorption on both Ni_{38} cluster and the

extended nickel surfaces is exactly the same. These computational results are qualitatively consistent with experimental results showing that binding of carbon to nickel clusters saturates quickly with cluster size (~n = 5) to bulk values. Our DFT results "over predict" the binding energies by approximately 50%. Nevertheless, the experimental results do not yield the relative site energies and these are felt by some to be important in nanotube nucleation and growth.

In another series of calculations,[6] we considered small, flattened "flakes" that may be viewed as having been cut from an unrolled nanotube. The flakes are two-dimensional, and none of the strain energy due to rolling was included in the calculations. Initially, we followed Lee et al.[7] and chose a flake consisting of five pure carbon hexagons. After establishing that our results agreed well with those of ref. 7, in which similar computational approaches were employed, the flake size was cut down to three hexagons (^{14}C atoms) so that a large number of calculations could be carried out on an accelerated basis. The agreement between results for the five and three hexagon calculations was excellent. The main reason for this agreement is probably that the carbon bonds, as in many organic systems, are quite well localized and therefore additive to a good approximation.

The initial set of calculations consisted of adding C, Cu, Au, Ni, Fe, and Co to form a closed pentagon. The main purpose of these calculations was to determine if there are any clear differences between metals that are good catalysts and those that are not. The binding energies, E_b, of these elements to the carbon flake fell into two well-resolved energy ranges, with E_b for Cu and Au about an eV less than for the other elements. These differences are too large and consistent with each other to be the result of the computational approximations that were made. Consequently, we view them as a reliable guide to the relative interaction energies of the metal atoms with the carbon flakes.

To take these considerations a step further, calculations were carried out to determine if a carbon atom and a metal atom on neighboring pentagon sites preferred to remain on those sites, as in Fig. 3(a), or to combine to form a mixed hexagon site and an empty pentagon site, as illustrated in Fig. 3(b). It was found that Cu and Au atoms preferred to remain on the separated pentagon sites, while Ni, Fe, and C preferred to form hexagons. This result can be used to substantiate the elementary catalytic step proposed in ref. 7, but space precludes our discussion of this here.

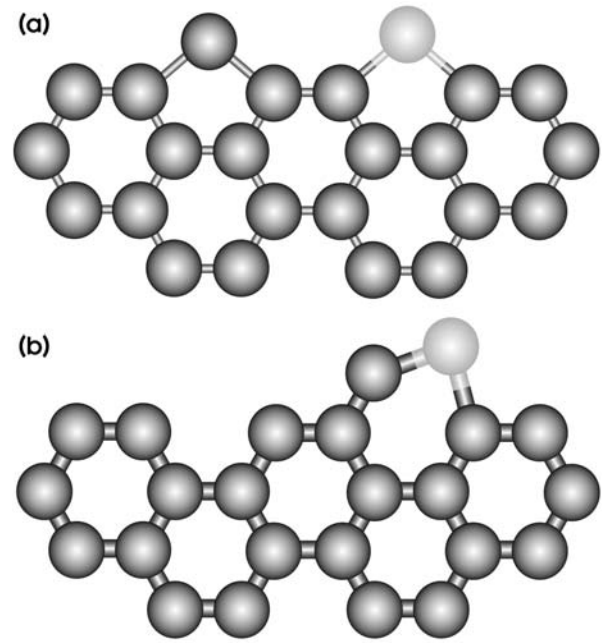

Fig. 3. Two separated pentagons, one with a carbon atom and one with a metal atom, as shown in panel (a), may combine to form the distorted hexagon in panel (b) if the total energy can be lowered in that way. Light circles are the metal atoms.

Summary and Conclusions

As part of a focused computational effort on the simulation of CNT formation, we have developed and applied computer programs for coupled heat and mass flow in one and two dimensions. The results clearly illustrate the crucial role carbon diffusion plays in the growth of nanotubes, and they explain a number of the experimentally observed growth phenomena. They also demonstrate the key roles played by the size and shape of the catalytic particle in conjunction with the concentration gradients at the gas/solid interface. While it is apparent that an impressive amount of insight can be obtained from continuum calculations, the need to go beyond this simple approach is apparent. We want to incorporate more effectively the input from first-principles electronic structure calculations and, working with experimentalists, to focus on the most reliable data obtained under well-defined conditions.

The binding of a carbon atom on various nickel surface and cluster facets was calculated. Small clusters yield the same results as extended surfaces. The Ni (100) facet is favored over the Ni (110) and Ni (111) facets. Electronic structure calculations of the binding energy of various metal atoms to a 14-atom carbon flake show that Au and Cu are less tightly bound than Ni, Co, and Fe by about 1 eV. Finally, comparison of the binding of a carbon and metal atom in a hexagon to the energy in separated pentagons indicates that for the catalytic metals the hexagon is stable against the breakup into two pentagons.

Preliminary results of the work described here were presented at the 2003 NASA/Rice Workshop on Single Wall Carbon Nanotube Growth Mechanisms. The

presentations were well received and have begun to establish ORNL as an important contributor to computational CNT research. The work on the continuum modeling has progressed to the point where significant concrete guidance can be given to the experimental efforts on CNT growth at ORNL. With continued development of the modeling and simulations, identification of the elementary catalytic step can be expected and with that a much deeper insight into how to control the growth conditions.

A white paper seeking follow-on funding was submitted to DARPA under one of their BAA solicitations. Submission of a full proposal was not encouraged, probably because of a weakness in the proposal not directly connected with the work reported here. The most promising avenue for follow-on funding is one that closely links the modeling to the experimental CNT effort at the CMSD at ORNL. Meanwhile, work on the modeling continues on a reduced level via funding from DOE's Office of Basic Energy Sciences.

References

[1]J. Alstrup, *Catal*. **109**, 241 (1988); R. T. K. Baker, *Carbon* **27**, 315 (1989); S. A. Safvi, E. C. Bianchini, and C. R. F. Lund, *Carbon* **29**, 1245–1250 (1991); R. T. K. Baker, *Encyclopedia of Materials: Science and Technology*, Elseiver Science Ltd., 932–941 (2001).

[2]P. Chitrapu, C. R. F. Lund, and J. A. Tsamopoulos, *Carbon* **30**, 285 (1992).

[3]S. Pannala and R. F. Wood, Proceedings of the NASA/Rice Workshop on Single Wall Carbon Nanotube Growth Mechanisms, *J. of Nanoscience and Nanotechnology* (in press).

[4]D. B. Geohegan, A. A. Puretzky, I. N. Ivanov, S. Jesse, G. Eres, and J. Y. Howe, *J. Appl. Phys*. (submitted).

[5]Q. M. Zhang, J. C. Wells, X.-G. Gong, and Z. Zhang, *Phys. Rev. B* (submitted 2003).

[6]J. C. Wells, D. W. Noid, B. G. Sumpter, R. F. Wood, and Q. Zhang, Proceedings of the NASA/Rice Workshop on Single Wall Carbon Nanotube Growth Mechanisms, *J. of Nanoscience and Nanotechnology* (in press).

[7]Y. H. Lee, S. G. Kim, and D. Tománek, *Phys, Rev. Lett.* **78**, 2393 (1997).

Development of Time-of-Flight Capabilities for Studies of Inelastic Neutron Scattering and the Dynamics of Soft Matter

P. D. Butler, W. A. Hamilton, and G. D. Wignall
Condensed Matter Sciences Division

Cold neutrons are a critical research tool for the investigation of scientific phenomena occurring on long (~ 5–1000 Å) length scales, and have been particularly successful for studies of "soft" matter such as polymers, complex fluids, and biological complexes. Over the past two decades, small-angle neutron scattering (SANS) has proven to be the most important technique for the study of such materials, revealing their structure on the nanoscale level, and it is well known that SANS instruments are the most over-subscribed facilities worldwide, attracting users from industry and government laboratories in addition to academic researchers. More recently, cold inelastic neutron scattering instruments have begun to come on line in this county to study the dynamics of these systems and are showing considerable promise. With the installation of a new cold source at the High Flux Isotope Reactor, this project's aim was to understand how to separate this dynamic information that must, in some cases, compromise regular SANS measurements, examining where that might be problematic, and perhaps more importantly to explore how SANS might be able to offer unique dynamical information, particularly for soft matter.

Introduction

To date, the treatment of SANS data has been based on the assumption that the scattering is predominantly elastic (i.e., the energies of the incident and scattered neutrons are the same) and the data may be integrated over all energies to give the time-averaged structure of the system. While this assumption is known to be true in the $Q \rightarrow 0$ limit, nearly all SANS experiments are conducted in the range $10^{-3} < Q < 1$ Å^{-1}, where the assumption of elastic scattering remains unverified. Moreover, those few studies in which energy analysis of the scattered beam has been performed indicate that this is not always a safe assumption. In 1999, for example, Rennie and coworkers found that in a number of common solvents (like water or toluene), inelastic SANS effects can be significant with *less than half* the 12-Å neutrons being scattered elastically as conventional SANS methodology assumes.[1] However, the motions on the nanoscale, which give rise to these inelastically scattered neutrons (i.e., scattered neutrons whose energy is different from that of the incident neutrons), hold important information about the dynamics (motions on the nanoscale) in the materials. Thus the goal of this project is to not only understand how inelastic "contaminations" may in some circumstances adversely affect our interpretation of SANS data and how to conduct experiments to avoid those pitfalls but also to open up new areas of physics by studying the inelastic component itself. In the process of working on developing the inelastic SANS technique, we identified several issues with the new class of detectors which ORNL has acquired for its SANS instruments. One of these has already led to the manufacturer developing an upgrade, while another is an ongoing concern both for the High Flux Isotope Reactor (HFIR) and spallation sources such as the Spallation Neutron Source (SNS). With ORNL building two best-in-class SANS machines, to rival the current best in Grenoble, France, the timely delineation of these critical issues will be invaluable to the success of the HFIR SANS program. As part of this project, we also developed a novel approach to dynamics using time-resolved SANS, which is discussed separately below.

Technical Approach

Although ORNL is building two state-of-the-art SANS machines, it does not currently have an operating SANS instrument. Thus all experiments were performed on the National Institute for Standards Technology (NIST) Center for Neutron Research (NCNR) SANS instrumentation in Gaithersburg, Maryland. The NCNR's SANS detectors are smaller than those which ORNL will use but are electronically identical. This new class of detectors provides an integrated data acquisition package. For historical reasons, NIST currently bypasses this, using instead its own acquisition electronics. Those electronics are inadequate for the purpose of inelastic measurements so that one of the requirements of this work was the implementation at NIST of this new integrated acquisition package, with its new time-stamping capabilities, to match

the anticipated ORNL configuration. The NCNR's aging electronics are obsolete, and in fact some critical components are no longer available. Thus the NCNR will eventually need to convert its electronics, making this a natural interagency collaboration.

Inelastic SANS

For purposes of this development program, we used simple optical choppers placed at the sample position to provide a time = 0 (T0) stamp on the neutrons. By measuring the arrival time of each neutron relative to that T0 and knowing the distance from the chopper to the detector, the energy of each neutron can be computed. The energy gain or loss can then be determined from the known incoming neutron energy provided by the upstream velocity selector. Only those neutrons arriving with zero energy change are elastically scattered, while all others are inelastically scattered. In order to provide the necessary pulse of neutrons, the optical chopper wheel was covered with cadmium (Fig. 1) containing two 2-mm-wide slits diametrically across from each other. In order to obtain reasonable time resolution, the 1.27-cm-diameter incoming beam was masked by cadmium containing a 2.5-mm-wide slit, making the incident beam 2.5 mm × 12.5 mm. The chopper was usually run at 40 Hz for a chopped beam of 80 Hz, providing a neutron-pulse width of roughly 0.3 ms FWHM. The chopper output timing signal was conditioned by feeding it through a pulse delay generator prior to sending it to the T0 input of the detector (Fig. 2). A routine implementation on a SANS instrument would provide a chopper package optimized for the geometry of the problem along with appropriate shielding. The instrument design implications are that sufficient space be available at the sample position for the insertion of such a device.

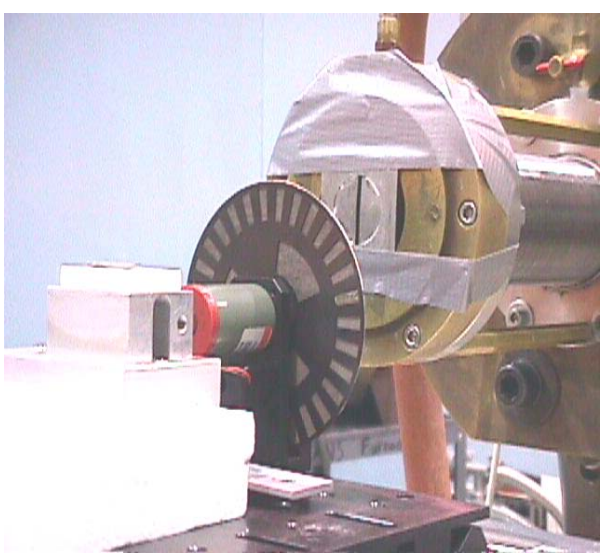

Fig. 1. Chopper and beam definition setup used for the inelastic measurements.

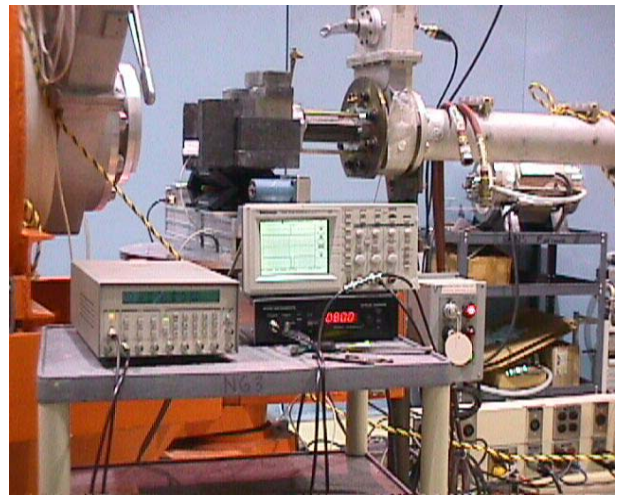

Fig. 2. Beam line operating with the chopper and signal conditioning electronics during the inelastic SANS run producing data such as shown in Fig. 3.

Time-Resolved SANS (T-SANS)

In order to do time-resolved SANS, the scattering signal must be time multiplexed into a series of histograms. The multi-time-binned SANS data collection is then cycled to build up statistics, synchronized at constant delay with respect to some experimental signal, in this case the stopping signal of our Couette shear cell motor. Given adequate electronics, the time resolution limit will be determined by the neutron time of flight and the wavelength spread in the incident beam and can extend down to hundredths of seconds, though duty cycles will usually be a more stringent limitation. It should be noted that our SANS direct neutron energy analysis experiments synchronize on a faster chopper phase signal, but in most respects the data collection issues of the two experiments are virtually identical so that lessons learned about data acquisition strategies from one set of measurements applies fairly directly to both techniques.

Time-resolved measurements have never been done with any significant resolution (i.e., more than 16 histograms) in the United States. Ideally, the new integrated acquisition system would provide nearly infinite histograms. However, as discussed below, implementation of the time-resolved modes of this acquisition package presented several challenges. Thus, in order to perform these measurements in a timely fashion, we opted for the creative approach of modifying the older, established electronics and acquisition software used at NIST. Specifically, the 128 × 128 detector pixel array of the two-

dimensional NIST SANS detector was rebinned in hardware into a 32 × 32 array, thus swapping spatial resolution for time resolution, giving us 48-constant-bin-width time channels. On the software side, we altered the indexing of the data arrays read into the live image display so as to be able to monitor our experiment in real time. In order to analyze the data, however, we opted to modify the ORNL SPECTOR software developed by John Hayter and Bill Hamilton for the old SANS at HFIR, as it is probably still one of the most versatile and well-designed acquisition/reduction packages available.

Results and Accomplishments

Acquisition electronics implementation

While this was simply a necessary by-product of the work, it produced several immediate benefits to the ORNL SANS program and so is described briefly here. The first obstacle encountered was the fact that the integrated acquisition system did not allow for external control (by, for example, an instrument computer), the programming assumption apparently being that the instrument would be controlled by the detector. Having identified the problem, we teamed with NIST to insist to the manufacturer that neither of us could operate in this mode. The availability of a live beamline at NIST to test the solutions allowed us to realize fairly quickly that the first simple solution was not robust enough for heavy user operation. While the final solution is still being tuned, the immediate benefit to ORNL and NIST is clear.

The discovery that these new detectors have a single input signal, programmed as a T0 reset signal was a second issue uncovered by this portion of the program. In this case, the NCNR's needs were more immediate and a solution was offered whereby this signal could be converted to an inhibit (or gate) input signal. This gate signal is normally used during routine SANS operation. However, time-of- flight applications, such as required for inelastic measurements, require the initial T0 signal, preferably with a gate signal also available. Converting the single input from gate to T0 and back is tedious and of course never provides both signals simultaneously. While we eventually took data with only a T0 input signal, future, more sophisticated implementations, both at HFIR and at NIST, will need both. Furthermore, spallation-source SANS instruments will probably want to use both signals routinely. Again working with NIST and the manufacturer, an upgrade board for these detectors has just recently been released which provides four inputs, two of which come factory programmed, one as a T0 and the other as a gate. ORNL has already purchased the upgrade for both its detectors, while NIST's most recently ordered detector was just delivered with the new board, making this another clear immediate benefit from this work.

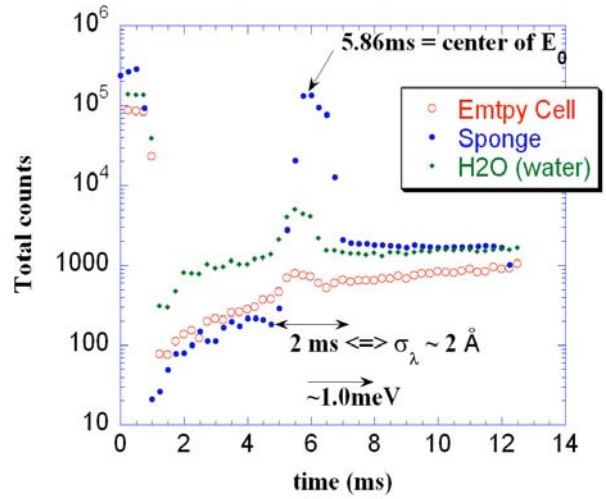

Fig. 3. Time-of-flight spectrum for three samples. The data represents the integrated counts overall the detector at each time. The filled circles are for a surfactant sponge sample, the filled diamonds a hydrogenous water sample, and the open circles an empty quartz cell. The incident wavelength used, λ, was 6 Å with a wavelength spread, λ/Δλ, of 10%. The effective time resolution is of the order of 2ms, making the wavelength resolution roughly 2 Å. The large central peak is the elastic signal. The energy resolution at the elastic peak is roufhly 1 meV. Note the abnormal behavior at short times.

Inelastic SANS

Figure 3 shows a time-of-flight spectrum of the whole detector integrated intensity (making this a low-*Q* resolution plot) for three different samples. The surfactant sponge sample was one of those used in the time-resolved SANS experiments to measure the energy of formation of passages and was hoped to show some evidence of the dynamic equilibrium of creation and disintegration of passages. The water sample is measured because it is known to have significant inelastic scattering and so serves as a test sample, while the empty quartz cell is expected to be a pure elastic scatterer to be used as a background. The incident wavelength used, λ, was 6 Å with a wavelength spread, λ/Δλ, of 10%.

The resolution of the measurement indicates roughly 1 meV. This can be improved with the use of a second counter-rotating chopper placed upstream to lower the effective wavelength spread. However, as can be seen, the data at higher energies than the elastic peak behave very oddly indeed. Unfortunately, due to the low energy of the cold neutrons, the energy gain side is the most likely place to see effects. It appears that the first 1 ms of data, regardless of configuration or time resolution used, contains a signal spatially identical to that in the elastic time bins, with a constant high intensity not related to the intensity of the elastic scattering. This seems to be somehow compensated for by having the time bins above 1 ms but below the elastic peak drop nearly to zero and

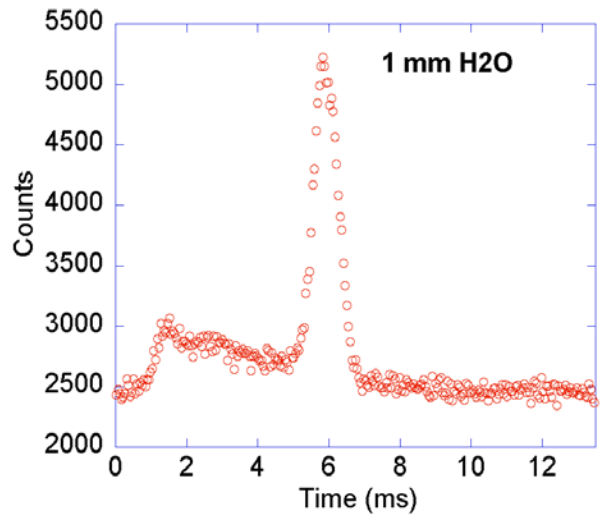

Fig. 4. Plot of the detector anode signal as a function of TOF for the same hydrogenous water sample as in Fig. 3. Note the difference in the low time behavior, with this data exhibiting the expected peak at short times.

come up only slowly. Figure 4 shows the water signal measured simultaneously by running the detector anode signal through a multichannel scalar. The resulting spectrum is exactly as expected with no intensity at 0 time (infinite energy) and significant inelastic scattering between 2 and 6 ms—with at least 2 peaks being easily discernable. This gives us reason to believe that the problem lies not in the detector itself but in the encoding done within the electronics. This issue has yet to be resolved. However, we note that this problem is not only important to ORNL SANS being able to provide inelastic capabilities, but it will also prevent us from doing T-SANS with this acquisition package, and of course precludes the use of the current integrated electronics with any spallation source such as the SNS SANS.

Time-Resolved SANS

Whereas normal SANS reveals the structures within materials, inelastic and quasi-elastic experiments reveal information about the dynamics within these materials. This is usually accomplished by measuring shifts in the scattered wavelength at each Q. The wavelength change reveals the energy involved, or equivalently the time scales, while the Q position speaks to the length scale of the motion. For much longer time scales, depending on the wavelength spread and distance from sample to detector (giving an effective TOF resolution), it is possible to measure some motions down to the hundreds of milliseconds resolution directly in the time domain as discussed previously. While a handful of such measurements of been reported on SANS machines worldwide, we are the first to relate the time sequence of structures back to an energy. Here we perform a time-resolved relaxation study of a shear-induced smectic surfactant membrane phase (L_α) transforming to its thermodynamic equilibrium sponge state (L_3), as shown in Fig. 5 with a time resolution of 0.2 s. Comparison of the T-SANS relaxation measurements with dynamic light scattering measurements of the pure diffusive membrane mode frequencies in this system (see figure) allowed us to determine the inelastic activation energy for the formation of the interconnecting "handles" which characterize the topological rearrangement of membranes required between these two states. This was in fact the first direct determination of the energy of this membrane fusion mode and the result, $E_A \approx 8k_BT$, was in excellent agreement with theoretical predictions for this system.[2,3]

Despite the rather rapid time sequencing used here, the motions in the normal sponge systems are still much too fast for these measurements. In order to perform this study, we therefore also employed the novel approach of using sugar as a viscosity enhancer, slowing the dynamics into an experimentally accessible region. This technique of adding sugar to slow the dynamics has now already been used by our Australian collaborator's Ph.D student working with gel systems while we are exploring it as an avenue to understand microemulsion behavior.

Summary and Conclusions

The modest progress in performing true inelastic measurements, with results showing better than 1 meV resolution, has generated significant interest both at ORNL and at NIST, and even other at facilities for that matter, and it is highly likely that this effort will be picked up by several groups, including our own. Meanwhile, the slow progress on getting the integrated acquisition package up

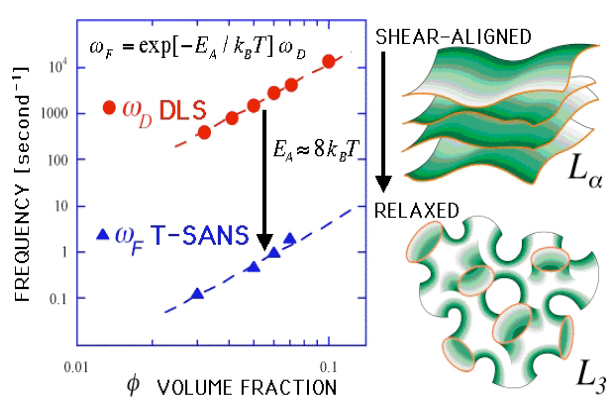

Fig. 5. Frequencies measured by both light scattering and T-SANS over a range of membrane concentration in a surfactant sponge phase and how the two are related through the energy of formation of handles which is thus determined.

and running on a NIST instrument provided both time to explore T-SANS as a new approach to SANS dynamics, which appears to hold tremendous promise, and vital information on the performance characteristics of the integrated acquisition system of the new class of detectors, which has already impacted the ORNL and NIST SANS programs as well as future SANS instrumentation worldwide, particularly at spallation sources.

The T-SANS work, along with its creative use of sugar to slow the dynamics of complex systems, is perhaps the most exciting aspect of this work, and again has also already had an impact on other programs. The results are clearly impressive. Further, the combination of T-SANS with TISANE (time-integrated small-angle neutron experiments, invented at ILL and being developed at NIST) and true inelastic SANS should allow a truly wide range of time and energy scales to be probed.

The main obstacle to general use of T-SANS now, and eventually of inelastic SANS, is the lack of analysis tools for handling such data. In order to make these techniques available and allow them to have the impact they should will require a significant software effort. One of us (P.D. Butler) is currently the principal investigator on an NSF subproject proposal (submitted) to produce state-of-the-art SANS analysis software.

References

[1] R. E. Ghosh and A. R. Rennie "Assessment of Detector Calibration Materials for SANS Experiments," *J. App Cryst* **32**, 1157 (1999)

[2] L. Porcar, W. A. Hamilton, P.D. Butler, and G.G. Warr, "Relaxation of a Shear-Induced Lamellar Phase Measured with Time Resolved Small Angle Neutron Scattering," *Physica B* (in press).

[3] L. Porcar, W. A. Hamilton, P. D. Butler, and G.G. Warr, "Topological Relaxation of a Shear-Induced Lamellar Phase to Sponge Equilibrium and the Energetics of Membrane Fusion," manuscript in preparation.

Selective Catalytic Oxidation of Hydrogen Sulfide

T. R. Armstrong,[1] N. C. Gallego,[1] S. H. Overbury,[2] W. A. Shelton,[3] X. Wu,[1] and A. K. Kercher[1]
[1]*Metals and Ceramics Division*
[2]*Chemical Sciences Division*
[3]*Computer Science and Mathematics Division*

Processing gas streams that produce hydrogen from fossil fuels commonly contain impurities, such as hydrogen sulfide (H_2S), which can poison shift catalysts and fuel cell electrodes if not removed. The removal of sulfur in these feedstocks by applying advanced desulfurization technologies is desired. The mission of this project was to evaluate one very promising technology, selective oxidation of H_2S to elemental sulfur on an activated carbon catalyst. The objective was to develop a fundamental understanding of the H_2S oxidation process on activated carbon catalysts, while further developing an understanding of the role of microstructure and surface chemistry on the catalytic process.

Introduction

Hydrogen is commonly produced by reforming of natural gas; however, reformate contains impurities, such as hydrogen sulfide (H_2S), which can poison shift catalysts and fuel cell electrodes. Even a low concentration (a few ppm) of hydrogen sulfide dramatically shortens the life of fuel cell catalysts. Major ongoing research efforts are seeking to develop fuel cell catalysts that are more sulfur tolerant. The mission of this research program was to develop an oxidative process to reduce sulfur levels to the parts-per-billion range using low-cost carbon-based catalysts.

Catalytic partial oxidation of H_2S using activated carbon as catalyst has been identified as a highly promising approach for reducing sulfur (H_2S) from well gas, fuel cell feedstocks, and hydrodesulfurizer streams down to ppb level. While activated carbons are commercially used for hydrogen sulfide removal from gas streams, the key mechanisms for H_2S removal and the critical features in an activated carbon catalyst are not well understood. Further, current removal strategies are strictly limited to adsorption of the sulfur species on the carbon followed by replacement and disposal of the spent carbon. Research efforts often have relied solely on commercial activated carbons, and none of the past development efforts have evaluated the use of carbon as a catalyst. In addition, the results reported by various investigators are often diverse and contradictory, especially concerning kinetics and reaction pathways. This project, therefore, aimed to develop optimized schemes for producing activated carbon catalysts by materials processing, molecular modeling, reaction mechanism studies, and engineering evaluation and to give new insights for the reaction mechanisms for the oxidation process in question.

Technical Approach and Results

The assembled research team allows for a processing-to-product approach to tackle the timely issue of hydrogen sulfide removal from reformate feedstocks of hydrogen. The feedback between materials processing, molecular modeling, reaction mechanism studies, and engineering evaluation provides a synergistic approach for the development of an activated carbon catalyst.

Different precursors and variations in activation conditions can produce dramatically different microstructures in carbon materials. A focused effort to identify their relationships and the influence of the resultant pore structure (pore volume, pore size, and distribution) on the performance of carbon catalyst was necessary. Surface functional groups play an important role in the catalytic activity of the catalyst; thus, it is important to identify the initial surface functional groups and then develop techniques to modify or alter surface functionality. To produce an optimal activated carbon catalyst, the functional group content should be tailored to optimize hydrogen sulfide adsorption and minimize side reactions, such as adsorption of CO and H_2O, that could result in the formation of release sequestered hydrogen sulfide products.

Inorganic impurities have also been shown to strongly catalyze hydrogen sulfide oxidation. In order to understand the influence of catalytic impurities on the reactions of interest, highly pure carbons will need to be synthesized to isolate their effects. Inorganic impurities must also be added to activated carbons of in order to elucidate their role on adsorption and catalysis. It is commonly accepted that metal impurities in activated carbons play important roles in catalytic performance. Key issues that must be clarified include (1) identification of the reaction mechanisms associated with specific impurities, (2) the

activity and selectivity of those impurities, and (3) the efficacy of these impurities after extensive sulfur deposition and catalyst regeneration.

Reaction mechanisms were determined using a combination of catalytic reactor experiments on simple gas mixtures, in situ analytical techniques (such as DRIFTS), and molecular modeling. Together, these techniques can isolate individual gas-carbon reactions, explore competition between gases for reaction sites, determine the mechanisms for deleterious side reactions, and predict ideal carbon structures for H_2S removal. This combination of analysis methods provided multiple perspectives of catalyst reactions, ranging from idealized thermodynamic reaction predictions to measured catalyst surface interactions to an overall perspective of downstream gas composition. Key reaction parameters included temperature, pressure, oxygen concentration, H_2S concentration, water content, and the concentration of other impurities.

Ultimately, an activated carbon catalyst is only successful for hydrogen sulfide removal if it can perform to required concentrations in an actual reformate gas stream for a reasonable time period using a practical reactor geometry. A catalyst must remove and retain hydrogen sulfide in the presence of the wide range of impurities found in reformate feedstocks. Optimized activated carbon catalysts need to be tested on simulated reformate feedstocks of hydrogen. The potential of promising catalyst candidates for regeneration also needs to be explored. Partnering with laboratories and industry will be explored as a means to evaluate down selected catalysts on actual reformed gas streams.

The selective catalytic oxidation process can occur both continuously (i.e., simultaneous adsorption and oxidation of H_2S to produce S_n) or in a batch mode whereby the reaction is separated into adsorption step and a separate oxidation step. Thermodynamic calculations using a Gibbs minimization approach have been carried out to determine the stability of possible side reactions to for SO_2 and COS. The thermodynamic analysis of the reaction between hydrogen sulfide–contaminated mixtures of air or CO is complicated by the possible formation of numerous species in the gas phase, as well as elemental sulfur. The gaseous species include S_n (n = 1,…8), SO_2, and COS, in addition to the sulfur-free oxidation production H_2O and CO_2. With the inclusion of reactants, a total of eighteen species can be assumed to be present. For the continuous process, reaction of a reformat stream with CO and 1 wt % H_2S with the stoichiometric amount of oxygen required by the reaction

$$H_2S + \frac{1}{2}O_2 \rightarrow H_2O + S_n$$

results in incomplete oxidation. The degree of oxidation obtained in practice could be higher if consumption of oxygen in the formation of CO_2 were kinetically inhibited. The predominant reaction products are COS and SO_2. For the batch process, these calculations have shown that no SO_2 or COS will form below 150°C when CO is not present. Calculations with CO present still need to be done.

The porosity and carbon structure of several commercial and laboratory-created activated carbons were determined. A catalytic oxidation system, which can be used to test the activity and selectivity of carbon catalysts at different experimental conditions by using a FTIR to monitor effluent gas concentrations, was constructed and tested. Ongoing tests on activated carbons focus on effect of temperature (100–200°C) and gas composition (CO, CO_2, H_2O). A Diffuse Reflectance Infrared Fourier Transform Spectroscopy (DRIFTS) reactor, which is capable of in situ measurement at reaction temperature, was used to identify the change of carbon surface chemistry in various gas atmospheres. Ongoing studies on the interaction of CO or H_2S with activated carbon have provided positive support for this approach. The results will be very helpful for interpreting the reaction mechanisms of H_2S oxidation and undesired side reactions.

The porosity and carbon structure of several commercial and laboratory-created activated carbons have been determined. Typical results are listed in Table 1 and Table 2. The activated carbons are derived from different precursors (pitch-derived carbon, coconut shell carbon,

Table 1. XRD parameters of assorted commercial and laboratory-activated carbons

	Precursor	Interplanar spacing (nm)	Crystallite height (nm)	Crystallite diameter (nm)
Anshan 1000 m^2/g	pitch fiber	0.3667	1.127	1.775
Anshan 1500 m^2/g	pitch fiber	0.3660	1.134	1.803
Calgon Centaur 4x6	coal	0.3574	1.157	1.813
Calgon OLC 12x40	coconut shell	0.3662	1.080	1.810
Calgon OVC 4x10	coconut shell	0.3764	1.107	1.847
ORNL SMM-19	carbon fiber monolith	0.3742	1.058	1.757
ORNL SMS-48	carbon fiber monolith	0.3743	1.081	1.736
PICA G55C-1	coconut shell	0.3737	1.037	1.821
PICA VA507	coconut shell	0.3767	1.053	1.886
Westvaco Ultramicroporous	wood	–	–	1.720

Table 2. Pore structure characterization of assorted commercial and laboratory-activated carbons from nitrogen adsorption analysis

	BET surface area (m^2/g)	D-R micropore volume (cc/g)	D-A average pore diameter (Å)
Anshan 1500 m^2/g	1393	0.756	22.3
Calgon Centaur 4x6	1144	0.506	21.3
Calgon OLC 12x40	1110	0.506	21.3
Calgon OVC 4x10	884	0.391	19.7
ORNL SMM-19	1730	0.895	22.8
ORNL SMS-48	1404	0.619	20.7

coal, and low-ash charcoal) in order to determine the effects of common inorganic impurities. Also, preliminary experiments sought to accurately determine their functional group content.

An in situ study has been initiated to understand the interaction of gas species such as H_2S, O_2, and CO with carbon surface and interpret the reaction mechanisms of H_2S oxidation and undesired side reactions for the formation of COS and SO_2. A DRIFTS reactor which is capable of in situ measurement up to 500°C was used to identify the change of carbon surface chemistry in various gas atmospheres. A preliminary study on the interaction of CO with activated carbon has provided positive support for this approach, and typical results are shown in Fig. 1

Reverse Monte Carlo modeling has been applied to diffraction data to produce a theoretical activated carbon microstructure. By introducing select modifications to theoretical microstructures, carbon microstructural variables can be kept constant except for a specific feature of interest (functional group content, pore size, carbon structural order, etc.), and the effect of specific feature changes on the thermodynamics and kinetics of H_2S removal can be predicted. Slight modifications of these theoretical microstructures will later be used to model the behavior of actual activated carbons, by incorporating the measured microstructural features of activated carbons.

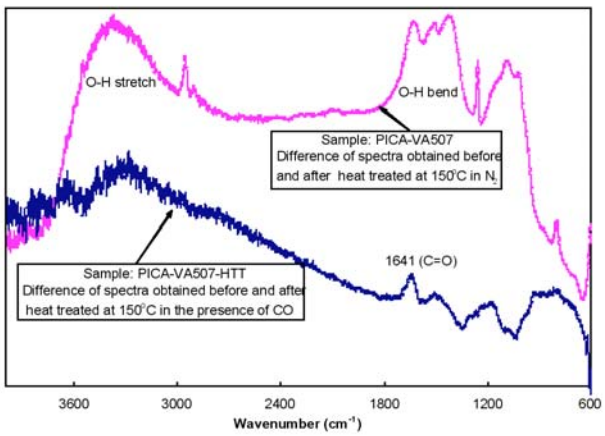

Figure 1. Preliminary results on the interaction of CO with activated carbon observed by DRIFTS.

Summary and Conclusions

This project demonstrated that H_2S can be oxidized and reduced by 99% in a single pass with little or no oxidation products being formed. Additional supporting theoretical and experimental data suggest that operation in a batch mode is preferred to ensure complete oxidation of H_2S and avoid formation of COS and SO_2.

Enhanced Performance and Energy Savings through Ultrahigh Magnetic Field Processing of Ferromagnetic Materials

G. M. Ludtka,[1] R. A. Kisner,[2] D. M. Nicholson,[3] J. B. Wilgen,[2] P. Kalu[4] G. Mackiewicz-Ludtka,[1]
G. M. Stocks,[1] and T. R. Watkins[1]
[1]*Metals and Ceramics Division,*
[2]*Engineering Science and Technology Division*
[3]*Computer Science and Mathematics Division*
[4]*National High Magnetic Field Laboratory, Florida State University*

This project is demonstrating and quantitatively documenting the influence of ultrahigh magnetic field processing on the phase equilibria and transformation kinetics for ferromagnetic materials. Novel microstructures with enhanced performance have resulted that inevitably will enable the implementation of new and lightweight materials that will lead to major energy savings and environmental benefits for the heat treatment and transportation sectors. A parallel simulation effort using modern first-principles electronic structure methods is being conducted to calculate the contribution to the free energy of the alloy phases that results from the application of these large magnetic fields. Based on the guiding principles established by this modeling effort, new compositions with their phase equilibria will be predicted and verified experimentally.

Objective

The broad goals for this research are to demonstrate and document the influence of ultrahigh magnetic field processing on the phase equilibria and kinetics for ferromagnetic materials and to develop predictive capability based on first-principles calculations. This ability to selectively control microstructural stability and alter transformation kinetics through appropriate selection of the magnetic field strength will be shown to provide a very robust mechanism to develop and tailor enhanced microstructures (even potential bulk nanostructures through accelerated product phase nucleation and transformation kinetics) with superior properties through a more efficient processing technology for a broad spectrum of material applications.

Technical Approach

The tasks and deliverables to successfully accomplish the objectives of this research include: (1) a predictive ultrahigh magnetic field processing simulation tool based on modern first-principles electronic structure methods and appended to a thermodynamic modeling software (ThermoCalc) with experimental validation; (2) quantitative experimental evidence of novel, ultrahigh magnetic field processed microstructures unattainable through conventional zero-field thermal processing methods; (3) ORNL capabilities for in situ characterization of magnetic field processing of materials; and (4) definition of future research thrust areas and funding resources for pursuing ultrahigh magnetic field processing as a major new ORNL research initiative. Of major importance to accomplish this research was the requirement to design and fabricate the first thermal-magnetic processing system for conducting ultrahigh magnetic field processing experiments in the U.S.A.

Results to Date

Significant progress has been made this past year in achieving these goals. These accomplishments will be highlighted under four subheadings defined as: Fe-15Ni Alloy, 52100 Alloy Steel, Bulk Amorphous Ferromagnetic Alloy, and Local Spin Density (LSD) Modeling.

Fe-15Ni Alloy: Experimental results on this INVAR-type alloy have quantitatively shown that magnetic field processing enables obtaining conventionally unachievable $\alpha + \gamma$ microstructures as exhibited by enhanced solid solution solubilities and phase distributions (volume fraction) compared with conventional equilibrium phase diagram data. Specifically, the γ phase Ni composition of a magnetically processed sample was 40 atomic percent for a 500°C heat treatment with an imposed field of 29 T compared to an equilibrium value of 30 atomic percent without a field. Similarly, the volume fraction of the α phase was magnetically enhanced by a factor of 2 to 28% compared to an equilibrium value of 14%.

52100 Alloy Steel: The application of a magnetic field at ambient temperature after an austenitization heat treatment and helium quench cycle resulted in an increase

in hardness of 14% when compared to a sample similarly processed but with no post quench magnetic field cycle. These results support the prediction that magnetic field processing raises the martensite start and finish temperatures of ferrous alloys and can enhance material properties. In addition, metallographic examination of other samples after various heat treatment cycles with a magnetic field imposed during continuous cooling from the paramagnetic austenite phase field indicates acceleration of the phase transformation kinetics, stabilization and enhancement of the ferromagnetic phases, and carbide precipitation normally only achievable with additional cryogenic processing.

Bulk Amorphous Ferromagnetic Alloy: Limited experiments this past year on a bulk amorphous ferromagnetic alloy annealed at 670ºC with and without an imposed 30-T magnetic field indicate an influence on the crystallization behavior of this material. These initial results suggest a potential impact of magnetic processing on the stabilization of precursors to ferromagnetic (or high susceptibility) phases which may allow for the formation of materials with unique magnetic properties.

Local Spin Density (LSD) Modeling: This task is enabling the prediction of phase diagrams accounting for the imposition of various magnetic fields while at elevated temperature. This past year the LSD model was modified to capture the coupling of volume and magnetic effects. This locally self-consistent multiple scattering, LSMS, code currently qualitatively captures the change in volume fraction of α and γ phases for the Fe-15Ni alloy system. The prediction of the shift in Ni concentration at which the α- and γ-phase free energy curves intersect indicates an increase in the martensite start temperature of this alloy and enhanced α phase stability as experimentally observed.

Benefits

Successfully demonstrating this novel materials and process development concept, while providing a fundamental understanding and predictive capability of the potential magnitude of the effects of this ultrahigh magnetic field processing technology, will result in significant future program and funding development interest from several major resources. The DOE OIT and OTT Programs definitely would fund additional technological development for this processing methodology. As an example, Dr. Peter Angelini, OIT Program Manager, indicated in a conversation that future funding under his Industrial Materials of the Future Program would be viable for further developing and implementing within industry this proposal's concepts once this initial research effort was completed. Similarly, the Department of Defense DARPA structural amorphous metals program would benefit from the phase destabilization and magnetic cooling aspects of this project to meet their goals of developing stabilized magnetic glasses. In addition, recent presentations to the U.S. Army Aviation & Missile Command in Huntsville, Alabama, have developed their interest in pursuing DARPA-funded magnetic processing research for ORNL for specific structural and aerospace applications.

Materials Science of Nanostructured Carbons and Graphites

T. D. Burchell,[1] J. W. Klett,[1] C. L. Fu,[1] N. Gallego,[1] J. Y. Howe,[1] M. K. Miller,[1]
D. B. Geohegan,[2] W. A. Shelton,[3] and J. Calo[4]
[1]*Metals and Ceramics Division*
[2]*Condensed Matter Science Division*
[3]*Computer Science and Mathematics Division*
[4]*Brown University*

The complex and disorganized structures of microporous carbons, in which the dimensions of the pore spaces are commensurate with the dimensions of the adsorbate molecule, make interpretation of adsorption very difficult. Indeed, our ability to advance the materials development is hindered by our lack of fundamental insight into the key structure-adsorption relationships. The objectives of this work are (i) the characterization of the nanostructure of a range of carbon materials, (ii) assessment of the H_2 storage capability of nanostructured carbons, (iii) the development of mathematical models that describe the "real" carbon structure and the interaction of H_2 with carbon and catalysts, and (iv) the application of those models to assess the nanostructure features that control the interactions of the carbon with the H_2.

A test matrix of ~20 different carbon samples, including commercial activated carbons, adsorbent carbon fibers and composites, graphite nanofibers, carbon nanowebs and single-walled carbon nanotubes (SWNTs), was assembled and characterized via N_2 adsorption at 77 K. Selected samples were examined for their ability to adsorb H_2 (at pressures up to 20 bar). The gravimetric uptake of H_2 adsorbed on the carbons tested increased with the surface area of the sample. At room temperature and 20 bar pressure, the maximum observed H_2 uptake was ~0.3% on a commercial activated carbon. This increased to ~6% at 77 K. Pure SWNTs exhibited an uptake of ~0.12% at room temperature and ~20 bar, increasing to ~6% at 77 K.

We used high-resolution transmission electron microscopy (HRTEM) to characterize SWNT purity and defect level before and after chemical purification. As-grown SWNTs may contain up to 50 wt % of impurities that mainly consist of the residual metal catalyst particles and amorphous carbon. HRTEM is an indispensable tool to evaluate the fine structures of the SWNTs at various stages, that is, as-grown and after purification. The availability of purified samples is key to determining whether H_2 adsorption on nanotubes samples is influenced by the presence of the metal catalyst. Contrast matching small-angle neutron scattering was conducted on microporous carbon monoliths to study the pore structure of the materials at nanoscale. Deuterated *n*-pentane was the matching agent as it is a chain-like molecule with similar neutron contrast to the carbon. It was found that the microporosity (<2nm) was all open porosity.

Using first-principles method, we have studied the binding interactions of H_2 molecules on the graphite surface with and without the presence of metal particles (e.g., Pd). First, without Pd, we find that H_2 molecules interact weakly with the graphite sheet (i.e., physisorption) with a low binding energy (0.08 eV); the H-H bond length is unaffected by the graphite surface. The adsorption of H_2 on the graphite surface is unlikely at room temperature (in agreement with our experimental evidence). Second, despite the strong in-plane C-C bond, Pd atoms can be adsorbed easily on the graphite surface. The H_2 molecule is found to bind preferentially to the Pd atom, with a binding energy as high as 1.36 eV (130 KJ/mole); the H-H bond length increases by 17% (with a sizeable reduction in the H_2 vibration frequency) with respect to that of the isolated H_2; that is, the presence of metal particles promotes the adsorption and dissociation of H_2. Third, while the electronic interaction between Pd and H_2 on the graphite surface is local, we find that a single Pd atom can promote the adsorption of up to six H_2 molecules on the graphite surface, indicating that the H_2 storage properties can be drastically improved even in the presence of a few metal particles.

We have additionally made significant progress toward devising a model for computing amorphous carbon structures from experimentally determined radial distribution data. To validate our approach, we have run a variety of test cases on other known amorphous carbon structures where we have successfully reproduced the structures. The simulations demonstrate that the structures are actually somewhat insensitive to the radial distributions

and that moderate broadening in the radial distribution peaks is accompanied by gross changes in the structure.

The ability to model the complex interactions between gases and nanoporous carbons will lead to an enhanced understanding of the physical adsorption process and guide the development of improved nanoporous carbon adsorbents. Such developments will support ongoing DOE programs, including research into the production and storage of hydrogen and methane, the separation and capture of carbon dioxide, the desulfurization of combustion and fuel gasses, and fuel cell research.

Moreover, improved nanoporous carbon adsorbents that can be made specific for certain chemical agents would be of great benefit in the individual/collective protection of personnel from chemical weapons threats.

Aberration-Corrected, Ultra-High-Resolution Electron Microscopy for Atomic-Level Characterization of the Structure and Chemistry of Nanophase Materials

S. J. Pennycook,[1] M. V. del Arco,[1] L. F. Allard,[2] I. M. Anderson,[2] and D. A. Blom[2]
[1]*Condensed Matter Sciences Division*
[2]*Metals and Ceramics Division*

The recent successful implementation of aberration correctors in two ORNL scanning transmission electron microscopes, coupled with the upcoming acquisition of a commercial version for the HTML user facility, puts ORNL in a strong position to develop advanced imaging techniques for the Transmission Electron Aberration-corrected Microscope (TEAM) programs. The goal of this project is to develop the necessary theoretical and computational groundwork for the simulation and interpretation of atomic-scale images and spectra enabled by these unprecedented instruments.

In the growing area of nanophase materials science, the ability to characterize structure and chemistry of individual nanostructures atom by atom has been a dream ever since the famous 1959 lecture of Nobel Laureate Richard Feynman, "There's Plenty of Room at the Bottom," which first predicted the importance of nanotechnology. In that lecture, Feynman explicitly called for improving the resolution of the electron microscopes of that day by two orders of magnitude, to 0.1 Å, through correcting the aberrations of electron lenses. We are now within striking distance of achieving Feynman's dream, and ORNL is strategically positioned among university, corporate, and government research laboratories in the United States and worldwide to capitalize on this potential due to recent and ongoing investments in sub-angstrom electron microscopy. ORNL will soon have three of the first aberration-corrected electron microscopes in the nation, and we expect to be the first in the world to achieve a 0.5-Å electron beam. However, the extremely rapid rate of instrumental development has far exceeded the pace of technique development. The necessary theoretical and computational groundwork for the simulation and interpretation of atomic-scale images and spectra enabled by these unprecedented instruments has not yet been developed. It is critical that work be supported now to achieve rapid application and maximum payoff of our new ultra-high-resolution characterization facilities for the new world of sub-angstrom imaging. To address these opportunities, this project is undertaking research goals that were unthinkable just a few years ago: simulation and interpretation of three-dimensional images of individual nanostructures, spectroscopic determination of the elemental identities and local electronic structure surrounding individual dopant atoms, and observation and catalytic clusters with atomic resolution and sensitivity. Furthermore, the necessary theoretical and computational tools are being developed for the simulation and interpretation of the atomic-scale images and spectra enabled by these unprecedented instruments. During FY 2003, progress was made in three areas as described below.

Development of Reliable Techniques for Simulation of Single-Atom Images in Nanostructured Materials

We have expanded our Bloch wave analysis of the imaging process to the larger apertures available with present and next-generation aberration-corrected scanning tunneling electron microscopes (STEMs). The image indeed becomes a direct image of the 1s Bloch states, as proposed by us previously based on analytical approximations to the image, and a paper has been submitted to the *Journal of Electron Microscopy*. In addition, it has become clear that the non-1s portion of the incident probe will become increasingly important with increasing aperture angle. We found that this part will allow three-dimensional (3-D) reconstruction by a new and direct method, depth sectioning, as described in the next section. We have also initiated the frozen phonon multislice algorithm, which is more efficient for some purposes, and have extended the code to sub-Ångstrom probes.

Development of 3-D Tomography at Atomic Resolution and Sensitivity

Initially, it was thought that 3-D information would need to be extracted from the dependence of the image intensity on thickness, based on accurate simulations. Although this is now feasible, based on the insights from the image simulations described above, we also investigated the possibility of selecting atoms at different depths simply by focusing on them directly. Simulations have confirmed that the depth resolution increases with increasing aperture angle but also that it is not negated by the tendency of electrons to channel along atomic columns. The simulations have led to the realization that both types of behavior are seen for any given probe, the ratio depending on aperture angle. Channeling dominates for small angles, the depth sectioning effect for large angles. Experimentally we have already achieved 4-nm depth resolution using a 0.7Å probe, and that result was submitted to *Nature*. Simulations show that our current system should be able to achieve 2-nm resolution. The next- generation STEM anticipated from the future TEAM program should improve this to 1 nm, and depth resolution at the atomic level would be possible in a future-generation instrument with an additional factor of two increase in aperture angle. This work led to three invited talks at this year's Microscopy Society conference and an invitation to speak on the depth sectioning concept at this year's TEAM workshop.

Development of Electron Energy Loss Spectroscopy with Ultimate Sensitivity and Resolution

For electron energy loss imaging, a *Physical Review Letter* has been published showing agreement between experiment and simulation at atomic resolution. Therefore reliable techniques are now available both for Z-contrast imaging and element-specific spectroscopic imaging. On the experimental side we have detected and identified individual atoms within a bulk material for the first time. The sample was specially grown and comprised lightly doped layers spaced 10 nm apart. Dynamical simulations have been performed and allow the atom depth to be determined by comparing the calculated and experimental EELS images. With increasing atom depth, as a result of beam broadening, signals from adjacent columns increase relative to that from the column that contains the dopant atom. These results are shown in Fig. 1 and have been submitted to *Science*.

Recently, DOE Secretary Spencer Abraham released the 20-year plan,"Facilities for the Future of Science: A Twenty-Year Outlook" (www.sc.doe.gov/Sub/Facilities_for_future/facilities_future.htm), which included as a high priority aberration-corrected electron microscopy. To quote from his remarks to the National

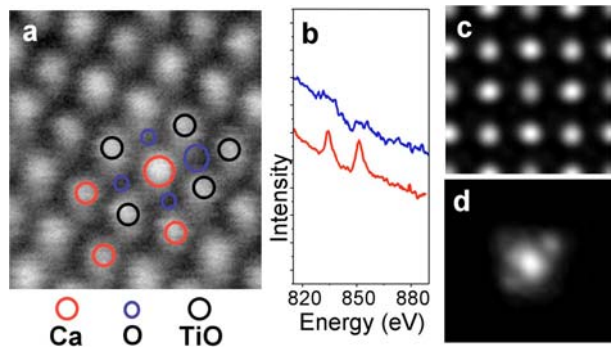

Fig. 1. (a) Z-contrast image of $CaTiO_3$ doped with a very low concentration of La. The column with the large red circle is on the Ca sublattice but is brighter than the other Ca columns, indicating the presence of a single La atom located within the specimen thickness. (b) EELS data from specific columns in the image identifying the La $M_{4,5}$ edge. A strong signal is obtained with the beam over bright Ca column, but a weak signal is also seen with the beam over the adjacent O column (large blue circle). (c) Simulated Z-contrast image with an aberration-balanced probe and 0.4 Å Gaussian broadening. (d) Simulated EELS image showing that significant La signal is anticipated from the adjacent O column due to beam spreading.

Press Club on November 10, 2003, "A new generation electron microscope can help us study how atoms combine to form materials, and how materials respond to external factors such as electric fields. This new instrument, the Transmission Electron Achromatic Microscope or TEAM, will help us design lighter, more efficient materials for everything from automobiles to advanced fuel cells." ORNL is an active participant inTEAM and already has two aberration-corrected instruments that represent prototypes for this next-generation instrument. This LDRD involves developing the methods of image simulation and analysis to support the capabilities of advanced hardware of this nature. We are developing advanced simulation tools to (1) quantify images at the ultimate resolution, (2) to reconstruct three-dimensional atomic structure from such images, and (3) to apply these advanced methods to energy problems of national interest. Such problems include materials science, catalysis, and nanoscience, which are high priorities for atomic-scale research with major potential for technological payoff to improve the nations economic well-being. Therefore this LDRD directly benefits many science and technology programs of DOE and other agencies.

Biologically Driven Controlled Synthesis and Directed Assembly of Nanophase Inorganic Materials

M. L. Simpson,[1] M. J. Doktycz,[2] T. E. McKnight,[1] and N. Samatova[3]
[1]*Engineering Science and Technology Division*
[2]*Life Sciences Division*
[3]*Computer Science and Mathematics Division*
University Collaborators
D. E. Morse,[4] G. S. Sayler,[5] J. J. Collins,[6] J. Turner[7]
[4]*University of California, Santa Barbara*
[5]*University of Tennessee Center for Environmental Biotechnology*
[6]*Boston University*
[7]*University of Tennessee Chemistry Department*

Our goal is to "learn the rules" of biologically driven controlled synthesis and directed assembly and eventually to apply these rules to the creation of engineered nanophase material systems. We are focusing ORNL's and our university collaborators' unique capabilities in biology, computation, and the nanosciences on mechanisms of biology that manipulate energy, information, and materials with spatial and temporal specificity on the nanoscale. As there are more than 60 different inorganic minerals produced by organisms from bacteria to humans, we could look at a wide variety of biological systems that synthesize inorganic nanophase materials. However, it was recently discovered in the laboratory of one of our collaborators that 'silicateins' (silica proteins) can be harnessed to direct the nanofabrication of other technologically important materials such as titanium dioxide, zinc oxide, and gallium oxide. This provides an appropriate model system to focus the science of this project while providing the potential of highly significant technology results. This work includes the following components: identifying/describing molecular processes useful for controlled synthesis and directed assembly of inorganic materials to create inorganic nanostructures abiotically; analysis, modeling, and simulation of natural gene/biochemical circuit and network topologies that control synthesis and direct assembly at the nanoscale in biological systems; the development of synthetic gene/biochemical networks for the engineered control/mimicking of biologically driven controlled synthesis and directed assembly; and the creation of nanoscale synthetic elements to deliver and control the expression of genetic materials within viable cells.

With a precision of nanostructural control that far exceeds present human capabilities, biological systems fabricate a remarkable diversity of three-dimensionally organized materials. Proceeding from instruction encoded within the genome to the completed nanostructures requires a set of complex processes that provides for the transport of material, energy, and information at the nanoscale that leads to the controlled synthesis and directed assembly of nanophase material systems. It is these processes, pathways, and complex network topologies that we are investigating. Stated in broad terms, our goal is to "learn the rules" of biologically driven controlled synthesis and directed assembly and eventually to apply these rules to the creation of engineered nanophase material systems. In FY 2003, we have made progress along several fronts as described below.

Molecular Processes Useful for the Controlled Synthesis and Directed Assembly of Inorganic Materials

Our principal objective has been to extend present expression and cellular display studies with the silicatein molecule on the surfaces of microbial cells to new and collaborative work on biofilms, in which the expressed silicatein molecules in microbial biofilms are used as structure-directing catalysts for the formation of oriented silica and siloxane-based nanostructured composite materials. Morse's lab succeeded in expressing silicatein alpha (the principal silicatein occluded in the biosilica needles produced by the marine sponge, *Tethya aurantia*) as a fusion protein with the bacterial surface protein, *OmpA*. This protein codes for a transmembrane protein that is produced in many copies and projects from the

surface of the bacterium, *E. coli,* into the surrounding medium. Morse's lab constructed the genetic fusion of the silicatein and *OmpA* genes in such a way to ensure that the silicatein sequence would be displayed in high copy number on the surfaces of the bacterial cells. When these bacteria were prepared as a film, and subsequently exposed to the silica precursor, TEOS (tetra-ethoxyorthosilicate) at neutral pH, the silicatein catalyzed the hydrolysis and subsequent polycondensation of TEOS to form silica. Evidence for silicatein/biofilm–directed templating of the silica synthesis was suggested by the close association of this silica with the microbial surfaces, but disappointingly, no higher-order regularity has yet been seen. Our further efforts to enhance nanoscale and higher-order regularity of the templated synthesis will be focused on: (1) optimization of conditions of synthesis; (2) use of organic silicon trialkoxides, to impose steric hindrance and other (e.g., pi-pi stacking) constraints on the degrees of freedom of synthesis; and/or (3) use of precursors of crystalline semiconductor metal oxides in place of the silicon alkoxides, to thus augment the structure-directing properties of the silicatein-containing biofilms.

Although limited by budget constraints, we were able to make some progress exploring the use of carbon nanofibers as templates for biologically driven synthesis. As a precursor to the use of silicatein enzyme systems, we have covalently attached soybean peroxidase (SBP) onto nanofiber scaffolding and validated the reactivity of the attached enzyme via colorimetric assay and precipitation visualization techniques. The homogeneity of the precipitant appears to increase if the immobilization reaction of SBP onto fibers is conducted following oxygen plasma etching of the fibers, apparently due to improved surface coverage of carboxylic acids and therefore SBP upon the fiber scaffold. FY 2004 for this thrust area is obvious: extend the vertically aligned carbon nanofiber derivatization work to the silicateins.

Analysis and Simulation of Gene/Biochemical Systems

We have developed an Exact Stochastic Simulator (ESS) which reads systems biology mark-up language (SBML) level 2 models and simulates biological models using the Gillespie algorithm with the Gibson and Bruck enhancements. ESS allows reactions to be specified using elementary rate constants or Hill Repression Kinetics. ESS was submitted and subsequently incorporated into BioSPICE version 2.0 as the standard stochastic simulator. Although the ESS tool is quite fast (with over 420,000 reactions per second achieved), computational demands for full cellular modeling vastly exceed this speed. To address this need, we developed a hardware accelerator we named FASST (FPGA Accelerated Stochastic Simulation Tool) which allows simulation of 4.5 million reactions per second—an increase in simulation speed of more than 10. To provide deeper insights into the structure/function relationship within gene/biochemical circuits and networks, we have developed a novel analytical approach that we refer to as the frequency domain chemical Langevin approach. In particular, compared to other noted gene circuit analysis, we find our approach leads to a deeper understanding of the architecture of gene circuits and networks and the emergences of robust behavior from systems composed of highly imperfect components.

This research directly addresses needs of DOE-BES programs in the design and synthesis of nanomaterials that focus on efficiently designing and fabricating materials "from the bottom up." Such challenging tasks are the essence of nanotechnology and materials science for the new century and therefore are a central focus of the DOE Nanoscale Science Research Centers. Additionally, the biological approaches pursued in this project accomplish the synthesis of nanostructured materials at relatively low temperatures, ambient pressure, at near-neutral pH, and in the absence of caustic chemicals, in marked contrast to present human manufacturing technologies. This provides a possible enabling technology for the controlled synthesis of nanoscale materials with a considerable energy savings and low environmental impact. This project aims to harness this capability for the abiotic production of nanoscale materials in direct support of DOE,s energy resources, and environmental quality missions.

Nanoscale Control of Collective Phenomena Using Artificially Structured Materials

H. N. Lee, H. M. Christen, and D. H. Lowndes
Condensed Matter Sciences Division

Advances in modern epitaxial growth techniques have enabled the synthesis of nearly perfect thin films, superlattices, etc., by the atomic-scale control of surfaces and interfaces. This enables the formation of artificial oxide superlattices that do not exist in bulk forms. During FY 2003, we have refined the growth techniques for metal-oxide heterostructures. Atomic-scale control of surfaces and interfaces led to the growth of epitaxial superlattices containing thousands of individual layers (at a total thickness of 1 micron) with extraordinary crystalline quality. Therefore, this capability now allows us to synthesize entirely artificial layered materials, combining dissimilar characteristics and leading to unprecedented physical properties.

Finding new physical phenomena at the nanoscale in complex metal oxides, including ferroelectric, ferromagnetic, and multiferroic materials, and manipulating the resulting properties in specifically designed epitaxial heterostructures, is a key challenge in ORNL's Condensed Matter Sciences Division. Epitaxial, artificial superlattice materials constitute a significant element of this research; however, many technical and scientific challenges related to their synthesis remain to be addressed. During FY 2003, most of the effort of this project was thus focused on the preparation of single-stepped substrates and the growth of conducting ruthenates as well as dielectric heterostructures by pulsed laser deposition (PLD).

As a first step, atomically flat, single-stepped surfaces were prepared on commercial strontium titanate ($SrTiO_3$) substrates using combined chemical (buffered hydrogen fluoride etch) and thermal treatments (at 1100–1200°C in air). Thin films of particle-free, atomically flat, electrically conducting $SrRuO_3$ were subsequently grown by a novel quasi-eclipse technique. In addition, the thermal stability of single-stepped epitaxial $SrRuO_3$ thin films (as required for subsequent growth of dielectric heterostructures) was explored as a function of temperature (25–800°C) and oxygen pressure (10^{-7}–10^{-2} Torr) by ex situ reflection high-energy electron diffraction (RHEED), low-energy electron diffraction (LEED), atomic force microscopy (AFM), scanning tunneling microscopy (STM), and X-ray photoelectron spectroscopy (XPS). We found that the decomposition mechanism of $SrRuO_3$ (yielding metallic Ru at the surface) is thermally activated with the activation energy E_a = 63 kJ/mol. A stability region was thus identified for the growth of dielectric materials on top of these electrode layers, and AFM, TEM, and X-ray investigations demonstrated the near-perfect transfer of crystalline structure from substrate to dielectric material through these $SrRuO_3$ films.

For artificial heterostructures, asymmetric tri-color superlattices (TCSs) with a combination of $BaTiO_3$/$SrTiO_3$/$CaTiO_3$, in which the inversion symmetry can be broken by a composition gradient, have been grown on $SrRuO_3$/$SrTiO_3$ substrates at 720°C in 10 mTorr O_2 (i.e., within the above-determined stability region). The controlled growth of artificial crystals in the form of epitaxial superlattices containing thousands of individual layers led to atomically flat surfaces even at a total thickness of 1 micron. This capability, therefore, gives us the freedom of materials choice in the design and synthesis of a multitude of multilayers containing materials with dissimilar properties.

Additional specific scientific observations during FY 2003 include (1) the first observation of spiral growth in a single-perovskite and the unambiguous correlation of these features with merging terraces on the $SrTiO_3$ substrates (bulk screw dislocations), and (2) the growth of submicron-sized oxide islands of an insulating perovskite on a conducting layer, by careful control of the growth mode.

During FY 2004, magnetic and multiferroic materials consisting of ferroelectric and ferromagnetic layers will be grown and tested by employing the growth technique established during FY 2003, in particular to investigate the charge and orbital ordering, ferromagnetism, ferroelectricity, and magnetic control of ferroelectric properties (or vice versa).

Such materials being investigated are highly relevant to DOE missions and will impact many federal agencies because of their potential usefulness for sensors, actuators and related devices. Thus, they may contribute to the entire range of security, energy, environmental, and science applications.

Materials Needs for Successful Implementation of Lean NO_x Treatment Technology

C. K. Narula,[1] L. F. Allard,[1] C. Goralski,[2] and C. S. Daw[3]
[1]*Metals and Ceramics Division*
[2]*Ford Motor Company*
[3]*Engineering Science and Technology Division*

The regulatory requirements for diesel emissions (excluding particulates) can be met by deploying NO_x trap systems (LNTs) for exhaust treatment; however, the performance of LNTs deteriorates rapidly. There is experimental evidence that repeated regeneration cycles (especially sulfation-desulfation) and associated high-temperature exposure of trap materials leads to the deterioration of LNT performance. Therefore, it is essential to understand the microstructural changes in trap materials associated with LNT performance deterioration. Such information is necessary for systematic research of new materials that can withstand the harsh conditions of regeneration cycles and, therefore, could lead to enhanced durability of LNTs. In this report, we describe our collaborative programs initiated to address the LNT durability issues and a summary of technical accomplishment of these programs.

The introduction of diesel engine or lean-burn-engine-based passenger vehicles depends on a successful development of a strategy to treat nitrogen oxides (NO_x) emissions, since a catalyst (or a combination of catalysts) that can convert NO_x into inert gases under oxidizing conditions over a complete range of exhaust temperature does not exist. Among NO_x treatment strategies, LNT are the most likely candidates for early deployment because they are consumer transparent and can be easily system integrated into current vehicle control strategies. However, several materials issues related to LNT aging need to be addressed before LNTs can be deployed in mass-produced diesel /lean-burn gasoline-powered vehicles. This research program is focused towards identification and alleviation of aging-related materials issues.

During the first year of this project, we investigated two issues: (1) microstructural changes in LNT materials under lean and rich conditions at high temperatures and (2) improving high-temperature durability of LNT materials.

Microstructural Changes in LNT Materials

A complete electron microscopic analysis of supplier catalyst aged under lean, rich, and stoichiometric conditions on a pulsator for lean gasoline conditions shows some interesting features:

- The fresh sample is a two-layer system on a honeycomb cordierite substrate. The inner layer is Pt/BaO-Al_2O_3, and the outer layer is CeO_2-ZrO_2. There are alumina islands in CeO_2-ZrO_2 layer that contain some barium. A dark field image of the CeO_2-ZrO_2 layer shows bright areas for the alumina islands and dark spots for segregated zirconia. This segregated zirconia is present only in fresh sample and is not seen in any of the aged samples. This suggests that segregated zirconia reacts with the CeO_2-ZrO_2 during aging. Since CeO_2-ZrO_2 forms under moderate conditions and crystallizes in a cubic fluorite phase regardless of ratio, the reaction of segregated ZrO_2 with CeO_2-ZrO_2 is not surprising. The dark field image of BaO-Al_2O_3 layer shows a uniform distribution of platinum particles. In general, platinum particles are about 5 nm. There is no indication of platinum or barium in CeO_2-ZrO_2 layer.
- The two layers in lean-aged samples remain intact. The segregated zirconia in CeO_2-ZrO_2 layer, seen in the fresh sample, is no longer segregated. The representative platinum particles, seen in the dark field image, have considerably increased in size as compared with fresh samples. The partial migration of barium from BaO-Al_2O_3 layer to CeO_2-ZrO_2 layer can be inferred from the EDS of an area near the outer edge of the CeO_2-ZrO_2 layer.
- The microstructure of a rich-aged sample is identical to that of the lean-aged sample. The aging under stoichiometric condition leads to partial migration of barium from BaO-Al_2O_3 layer to CeO_2-ZrO_2 layer. The sintering of platinum particles also occurs, but the extent of sintering is smaller than that under lean or rich conditions. (Note: the stoichiometric conditions refer to condition under which three-way catalyst operates in current gasoline-powered passenger vehicles.)

Thus, there are two pathways that can lead to reduced platinum–barium oxide contact. The increase in platinum particle size due to sintering reduces the number of catalyst sites that are available and in contact with barium oxide. The partial migration of barium into CeO_2-ZrO_2 leads to reduced barium in alumina layer that can be in contact with or in close proximity of platinum. Both pathways occur during lean or rich aging of LNT catalysts.

Model Catalyst Materials with Improved Thermal Durability

The complexity of the LNT described above warrants a complex model system that can be analyzed and evaluated in laboratory. Improvements in the model system then can be implemented in the full-size catalyst that can be tested on a vehicle. While at Ford, CKN started addressing the thermal durability of LNT materials. He found that a model system [10%CeO_2-ZrO_2-90%(2%La_2O_3-98%BaO.6Al_2O_3)] retains its beneficial surface properties even after thermal aging at 1050°C. This material can be prepared as follows:

1. Impregnation of $Ba(NO_3)_3$ on commercial high-surface-area alumina, pyrolysis, and sintering at 750°C.
2. Impregnation of step 1 material with lanthanum nitrate, pyrolysis, and sintering at 750°C.
3. Ball milling step 2 material with commercial high-surface-area CeO_2-ZrO_2.

As a next step, we impregnated this powder with 1% platinum and investigated platinum distribution on the powder. The electron micrograph shows that platinum particles are about 1 nm in size.

Next Steps

We have recently completed the complete redesign of an ex situ reactor for rapid screening of LNT materials for their durability under operating conditions by monitoring microstructural changes using TEM. We have procured funding and purchased components to set up a bench-top flow reactor at NTRC to evaluate LNTs using simulated exhaust. The model materials and new materials that address aging issues will be evaluated on these two systems.

Catalysis is a major thrust area for DOE-EERE FreedomCAR and Vehicle Technologies (OFCVT). The ability to prepare, characterize, and evaluate new LNT materials under this program complements the DOE-EERE-funded diesel programs at NTRC on evaluation of LNT and HTML involvement in several catalysis-related efforts, generally addressing the changes that occur at the microstructural level in collaboration with Ford, Cummins Engines, Caterpillar, etc.

Production of Hydrogen Using Nuclear Energy and Inorganic Membranes

B. L. Bischoff,[1] C. W. Forsberg,[2] L. D. Trowbridge,[2] and L. K. Mansur[1]
[1]*Metals and Ceramics Division*
[2]*Nuclear Science and Technology Division*

The Iodine-Sulfur (IS) thermochemical process is the leading candidate worldwide for production of hydrogen (H_2) using nuclear energy. This process thermocatalytically cracks water yielding hydrogen and oxygen. The IS process consists of a series of chemical reactions where all the chemicals are recycled in the process except for water. The high-temperature chemical reaction in this cycle is the thermal decomposition of sulfuric acid. The IS process is efficient, scalable to large sizes, and uses no expensive chemical reagents. However, it has one major disadvantage: high operating temperatures (800 to 900°C). This is not a show stopper. There is potential to lower the peak temperature by more than 200°C if the high-temperature decomposition products of sulfuric acid can be separated using an inorganic membrane. Lowering the peak process temperature may (1) allow existing designs of high-temperature reactors to be used for H_2 production, (2) reduce development times for a nuclear-H_2 system by many years with the potential that nuclear H_2 is a relatively near-term option, (3) improve the economics, and (4) improve the safety of the process.

The goal of this project is to conduct proof-of-principle experiments and associated analysis to demonstrate the potential for inorganic membranes to dramatically improve the IS process. The challenges that must be overcome are the development of membranes that promote the separation of O_2, H_2O, and SO_2 from SO_3, testing under simulated conditions of the IS process, and development of a model that describes the separation of multiple species from a multicomponent gas stream. ORNL leads the world in development of inorganic separation membranes. The technology is based on the technology used in the gaseous diffusion uranium enrichment plants. If this technology can be shown to potentially lower the IS peak temperatures, ORNL would become a major player in development of technologies for generation of H_2 using nuclear energy and a major development effort supporting GEN IV reactors would follow.

The overarching objective of this project is to demonstrate that inorganic membranes can dramatically improve the IS process by lowering the peak temperature. Technically, this requires demonstration that inorganic membranes can be employed to separate O_2, H_2O, and SO_2 from SO_3 and that this separation will enhance the conversion of SO_3 to SO_2 and lower the temperature required for almost complete conversion by 100 to 200°C. Separation will be determined by measuring and comparing single-gas permeances. The measurements will be conducted at temperatures up to 600°C, and these results will be extrapolated to the expected operating temperatures of 650 to 750°C. These results will be incorporated into a model that is being developed by Sandia National Laboratory and General Atomics to show what effect inorganic membrane separations will have on the efficiency of the IS process.

Measuring the permeance of the gases, SO_2 and SO_3, involves some unique challenges. First these gases have a low vapor pressure. In order to operate at pressures up to 100 psig, the gas cylinders, piping and valves, pressure transducers, and flow meters all must be heated to over 100°C for SO_3 and to about 60°C for SO_2. Second, these gases are both corrosive and toxic. Selection of wetted materials is very important, as is minimizing the concentration of water vapor in the gas stream in order to maintain the integrity of the system piping and its components. However, safety was the most important factor that went into the design of the membrane test system. The system design was completed in July 2003 and is shown in Fig. 1. The complete system was designed to fit into an existing fume hood located in Building 4501. This lab had the necessary security systems to handle the testing of these sensitive membranes. The system design includes a chemical trap to minimize the possibility of any of these corrosive gases entering the fume hood ductwork and also includes a diluent gas stream to minimize their corrosivity. All the components compatible with both the gases and the high temperatures were ordered in July and August, the system fabrication was completed in October 2003, and system checkout is currently taking place.

Concurrently with the above work, a series of membranes was fabricated and characterized and are

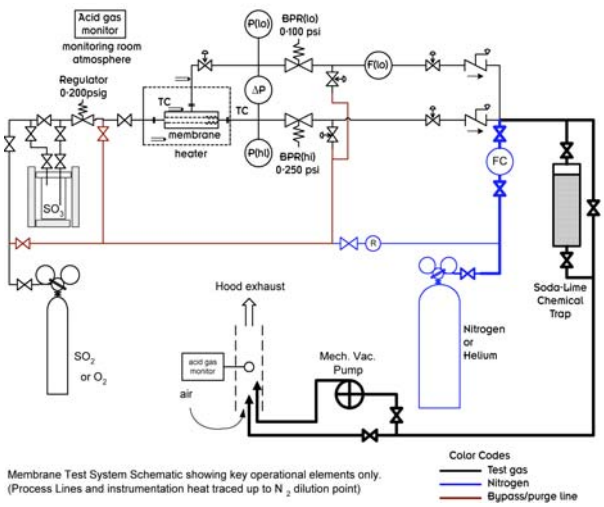

Fig. 1. Membrane test system schematic showing key operational elements only. Process lines and instrumentation heat traced up to N_2 dilution point.

candidates for initial testing in the system. The membranes were estimated to have pore sizes ranging from 0.62 nm to almost 0.9 nm.

A Research Safety Summary was completed and approved in August 2003, and the operational checkout of the test system should be completed in November 2003. Initial evaluation of the first-generation membranes by measuring the pure gas permeances at several temperatures will be completed by January 2004. Second-generation membranes will be fabricated and evaluated during the remaining months of FY 2004 using both pure gases and gas mixtures. These results will demonstrate that the ORNL membranes can have a major impact on the success of using nuclear energy to produce hydrogen.